Multipole method for modeling linear defects in photonic woodpiles

Dougal J. Kan,* Ara A. Asatryan, Christopher G. Poulton, and Lindsay C. Botten

Centre for Ultrahigh-bandwidth Devices for Optical Systems (CUDOS) and Department of Mathematical Sciences, University of Technology, Sydney, PO Box 123, Broadway, NSW 2007, Australia
**Corresponding author: Dougal.Kan@uts.edu.au*

Received August 28, 2009; revised November 8, 2009; accepted November 8, 2009; posted November 13, 2009 (Doc. ID 116339); published January 12, 2010

We extend the multipole method to allow for rod-type defects in woodpiles composed of infinitely long cylinders. A coupled-resonator optical waveguide and a linear waveguide are considered, where each waveguide is embedded in a woodpile cladding. For both structures, low-loss waveguiding is observed ($Q \approx 1\times10^4$–3×10^4). Decreasing the radius of the defect rod shifts the transmission resonances to shorter wavelengths. The reflection and transmission coefficients of the woodpile are derived for the case of normal incidence in the long-wavelength limit, and it is shown that both the individual layers and the entire assemblage of layers homogenize to one-dimensional dielectric slabs. Expressions for the effective permittivities are given. © 2010 Optical Society of America

OCIS codes: 260.0260, 260.2110, 260.2065, 050.0050, 050.1960.

1. INTRODUCTION

Photonic crystals (PC) are structures whose permeability and permittivity vary periodically on the wavelength scale [1,2]. This periodicity causes photonic bandgaps (PBGs) (i.e., frequencies for which the propagation of light is totally suppressed within a structure) to appear in the frequency bands of the modes of a PC. An important feature of PCs is their ability to localize light to structural defects by means of the PBG. While great strides have been made in the fabrication and analysis of PCs that are periodic in two dimensions (2D PCs), these structures are somewhat limited in that their PBG is only capable of confining light propagating in the plane of periodicity, and thus they must rely on total internal reflection to confine light propagating out-of-plane. By contrast, the PBGs of 3D PCs can be complete in that confinement is possible for all directions, thereby providing a means of virtually eliminating scattering losses. This provides a strong impetus to the investigation of 3D structures [3–5]. Unfortunately the development of 3D devices has been hampered by the complexities involved in accurately engineering a 3D PC. Further, while there are several invaluable numerical methods for modeling the behavior of PC devices [7,6], their generality prevents them from taking full advantage of the geometry of the problem, hence using them to model truly 3D geometries is often a prohibitively time consuming task.

Photonic woodpiles [3] are layered 3D PCs whose constituent layers are gratings and in which the rods of every second layer are oriented orthogonally to those of the layer immediately above or below, where it is usual for the periods in the x and y directions to be the same (see Fig. 1). It is instructive to regard the woodpile as a stack of pairs of orthogonal gratings where, so that there is a full bandgap, each successive pair is offset laterally with respect to the pair below, resulting in an interleaved structure. One advantage of the woodpile is that it can be produced in a layer-by-layer fashion using well-established techniques for fabricating 2D gratings (see, e.g., [8,9]). In addition, woodpiles have been made from a wide range of materials. These include woodpiles made from GaAs using wafer bonding [10], those made from metals using deposition methods [11], as well as those made from direct writing of polymers [12] and chalcogenide glasses [13]. The latter are of particular interest due to their high refractive index and highly nonlinear optical response. Wafer bonding techniques have also proven to be amenable to the incorporation of line defects [10], while direct writing can conceivably be used to create defects of arbitrary shape.

In this paper we describe how an existing multipole theory for woodpiles [14] can be extended to handle linear defects as well as disorder by generalizing the grating unit cell so that it can accommodate more than one cylinder (see Section 2). To demonstrate the method, we have computed the band structure of a woodpile along with the transmittance of a 28-layer woodpile containing a single defect layer. Two defect structures are considered; the first is a coupled-resonator optical waveguide (CROW) created by perturbing every second cylinder in the defect layer (see Section 3.A). It should be noted that a similar type of defect has been studied in earlier work [15], where the defect was a consequence of the fabrication process and was present in every layer of the woodpile. However, here we introduce a defect for the express purpose of creating a device layer. The second device that we consider is the more computationally demanding case of a linear waveguide formed by perturbing the central cylinder of the unit cell, as in Fig. 1, (see Section 3.B). We also illustrate the advantage of using a semi-analytic formulation by deriving expressions that show explicitly the behavior of the woodpile for normal incidence in the long wave-

0740-3224/10/020246-13/$15.00

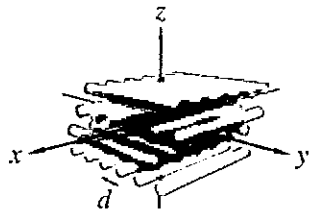

Fig. 1. (Color online) Photonic woodpile. A linear waveguide can be created by altering the properties of a single cylinder (red/dark cylinder).

length limit (Section 3.C), as has been studied previously in two-dimensions for finite stacks of cylinder gratings [16] and for square arrays [17]. We show that under these conditions the woodpile becomes largely insensitive to the polarization and behaves as though it were a uniform slab.

Other approaches that are commonly used in the study of woodpiles are the finite-difference time domain (FDTD) [6] and plane-wave expansion (PWE) methods [7]. Obtaining well-converged solutions with these methods, however, is difficult, even for the relatively simple case of a planar defect [18]. In comparison, the multipole method exploits the fact that, for stacks of gratings composed of cylinders, it is more appropriate to express the electromagnetic fields in terms of a rapidly converging basis of cylindrical harmonics. The multipole method can deal with planar defects with ease and is thus well suited to problem of modeling structures possessing complete PBGs, which, because of the strongly scattering environment needed to induce a complete gap, requires high-resolution sampling over the bandgap frequencies.

The requirement of having only cylindrical elements is not as limiting as it might seem. For purely theoretical considerations, the symmetries of the rod are of greatest significance, for example, in understanding how Q factors depend on defect position [19] or when analyzing loss mechanisms. Furthermore, direct writing methods have generated much interest recently [12,13,20] due to their ability to precisely inscribe arbitrary geometries into a wide range of host media. For example, inverse woodpiles consisting of a lattice of cylindrical tubes in a Germanium matrix were recently reported in [21]; the significance of this is that inverse structures induce much wider bandgaps. The structure fabricated by [21] theoretically has a complete PBG as large as 25%. We remark that our treatment can be readily adapted to handle noncylindrical scatterers by using a more general multipole framework, as has been done previously for conical mountings of finite 2D arrays [22].

In addition to the substantial efficiency gains afforded by the multipole method, the formulation presented here has a number of merits that are worth commenting on. While ostensibly it is a super-cell approach, it differs from other super-cell methods in that it requires periodicity only in the directions of the grating but not in the stacking direction and, thus, is appropriate for modeling structures that consist of a finite number of layers. This compares favorably with the PWE method, which instead employs a 3D super-cell. In [18], slight discrepancies between FDTD and PWE modeling were attributed to poor convergence resulting from using an insufficient number of layers in the super cell. Modeling waveguides embedded in a truly infinite cladding is also straightforward and permits the study of structures for which the only loss mechanism is lateral scattering within the waveguide layer. Metallic structures can be modeled by simply taking the refractive index to be complex. Finally, one more advantage of the multipole method is the possibility for tailoring the response fields of the rods to model a truly infinite grating [23,24].

2. THEORY

In this section we outline how to generalize the theoretical description of [25] to allow for gratings that contain more than one cylinder per unit cell, as shown in Fig. 2(a). Our treatment is analogous to that of [25]; the key difference lies in the form of the associated Green's function. When there is only a single cylinder, the polar representation of the Green's function is expressed in terms of *global* lattice sums that represent the field contribution due to the periodic replicates of the cylinder. For $N_c>1$ cylinders per unit cell, the polar representation also involves *local* lattice sums that derive from multiple contributions from all other cylinders in the unit cell and their periodic replicates. For a 2D treatment of the $N_c>1$ case, see [26]. We remark that [26] differs from the 3D treatment in that the electric (E) and magnetic (H) problems completely decouple for 2D grating stacks. Furthermore, the treatment in [26] is restricted to either TE or TM polarized diffraction, hence the resulting scattering matrices $\mathcal{R}$ and $\mathcal{T}$ are formulated to act directly on the longitudinal components of the electric and magnetic fields. For 3D problems it is instead necessary to write the fields as a superposition of TE and TM components, as in [25], and thus $\mathcal{R}$ and $\mathcal{T}$ act

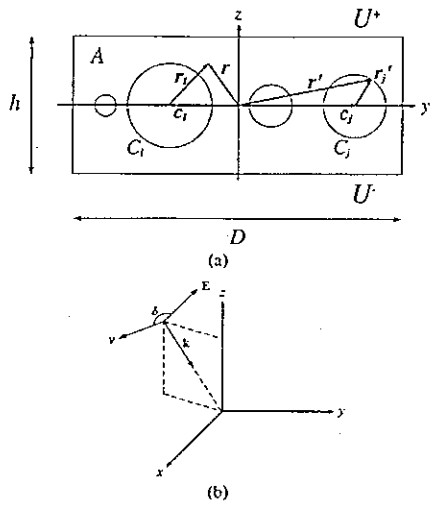

Fig. 2. (a) Up-down symmetric unit cell consisting of multiple cylinders that are aligned parallel to the x axis and whose centers lie along the y axis. The surfaces U^+ and U^- must be chosen so that the cylinders are completely contained inside region A. (b) Configuration of the incident field with wave vector k. The polarization angle δ is defined as the angle between vector $\nu=\mathbf{k}\times\hat{z}/(k\sin\theta)$ and direction of the electric field, with $\delta=0,\pi/2$ corresponding to TE and TM polarization, respectively.

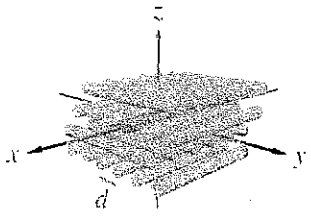

Fig. 1. (Color online) Photonic woodpile. A linear waveguide can be created by altering the properties of a single cylinder (red/dark cylinder).

length limit (Section 3.C), as has been studied previously in two-dimensions for finite stacks of cylinder gratings [16] and for square arrays [17]. We show that under these conditions the woodpile becomes largely insensitive to the polarization and behaves as though it were a uniform slab.

Other approaches that are commonly used in the study of woodpiles are the finite-difference time domain (FDTD) [6] and plane-wave expansion (PWE) methods [7]. Obtaining well-converged solutions with these methods, however, is difficult, even for the relatively simple case of a planar defect [18]. In comparison, the multipole method exploits the fact that, for stacks of gratings composed of cylinders, it is more appropriate to express the electromagnetic fields in terms of a rapidly converging basis of cylindrical harmonics. The multipole method can deal with planar defects with ease and is thus well suited to problem of modeling structures possessing complete PBGs, which, because of the strongly scattering environment needed to induce a complete gap, requires high-resolution sampling over the bandgap frequencies.

The requirement of having only cylindrical elements is not as limiting as it might seem. For purely theoretical considerations, the symmetries of the rod are of greatest significance, for example, in understanding how Q factors depend on defect position [19] or when analyzing loss mechanisms. Furthermore, direct writing methods have generated much interest recently [12,13,20] due to their ability to precisely inscribe arbitrary geometries into a wide range of host media. For example, inverse woodpiles consisting of a lattice of cylindrical tubes in a Germanium matrix were recently reported in [21]; the significance of this is that inverse structures induce much wider bandgaps. The structure fabricated by [21] theoretically has a complete PBG as large as 25%. We remark that our treatment can be readily adapted to handle noncylindrical scatterers by using a more general multipole framework, as has been done previously for conical mountings of finite 2D arrays [22].

In addition to the substantial efficiency gains afforded by the multipole method, the formulation presented here has a number of merits that are worth commenting on. While ostensibly it is a super-cell approach, it differs from other super-cell methods in that it requires periodicity only in the directions of the grating but not in the stacking direction and, thus, is appropriate for modeling structures that consist of a finite number of layers. This compares favorably with the PWE method, which instead employs a 3D super-cell. In [18], slight discrepancies between FDTD and PWE modeling were attributed to poor convergence resulting from using an insufficient number of layers in the super cell. Modeling waveguides embedded in a truly infinite cladding is also straightforward and permits the study of structures for which the only loss mechanism is lateral scattering within the waveguide layer. Metallic structures can be modeled by simply taking the refractive index to be complex. Finally, one more advantage of the multipole method is the possibility for tailoring the response fields of the rods to model a truly infinite grating [23,24].

2. THEORY

In this section we outline how to generalize the theoretical description of [25] to allow for gratings that contain more than one cylinder per unit cell, as shown in Fig. 2(a). Our treatment is analogous to that of [25]; the key difference lies in the form of the associated Green's function. When there is only a single cylinder, the polar representation of the Green's function is expressed in terms of *global* lattice sums that represent the field contribution due to the periodic replicates of the cylinder. For $N_c > 1$ cylinders per unit cell, the polar representation also involves *local* lattice sums that derive from multiple contributions from all other cylinders in the unit cell and their periodic replicates. For a 2D treatment of the $N_c > 1$ case, see [26]. We remark that [26] differs from the 3D treatment in that the electric (E) and magnetic (H) problems completely decouple for 2D grating stacks. Furthermore, the treatment in [26] is restricted to either TE or TM polarized diffraction, hence the resulting scattering matrices $\mathcal{R}$ and $\mathcal{T}$ are formulated to act directly on the longitudinal components of the electric and magnetic fields. For 3D problems it is instead necessary to write the fields as a superposition of TE and TM components, as in [25], and thus $\mathcal{R}$ and $\mathcal{T}$ act

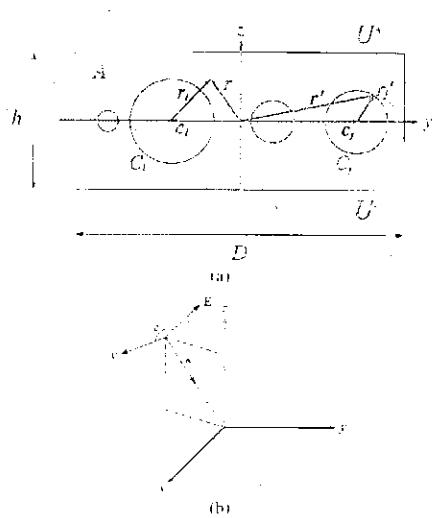

Fig. 2. (a) Up-down symmetric unit cell consisting of multiple cylinders that are aligned parallel to the x axis and whose centers lie along the y axis. The surfaces U^+ and U^- must be chosen so that the cylinders are completely contained inside region A. (b) Configuration of the incident field with wave vector k. The polarization angle δ is defined as the angle between vector $v = \mathbf{k} \times \hat{\mathbf{z}}/k \sin\theta$ and direction of the electric field, with $\delta = 0, \pi/2$ corresponding to TE and TM polarization, respectively.

on these components. In order to apply the multipole method, a change of coordinate system from *TE-TM* components to Cartesian components is then required. In all other respects, the derivation of the scattering matrices presented here parallels that of [26] with the exception that we do not require the magnetic permeability (i.e., μ) of the cylinders and the background region to be unity, thereby permitting the study of magnetic materials and, in particular, metamaterials.

The theory in this section is organized as follows. Section 2.A describes the procedure for obtaining multipole expressions for the fields produced by an up–down symmetric grating. In Section 2.B it is shown how to obtain the single layer reflection and transmission matrices by expressing the fields incident immediately above and below the grating in terms of the outgoing multipole coefficients. We briefly explain how the single-layer scattering matrices can be used to assemble the $\mathcal{R}^s$ and $\mathcal{T}^s$ matrices for a woodpile having a finite number of layers (Section 2.C). From these one can readily compute the reflectance and transmittance of the entire stack. In addition, they provide an efficient means of solving the fundamental problem of locating PBGs. An outline of how this can be achieved is canvassed in Section 2.D, where the propagating Bloch modes of an infinite woodpile are extracted from the scattering matrices of the stacking unit. While here we rely only on the Bloch modes to compute the band structure, they can also afford explicit equations for $\mathcal{R}^s$ and $\mathcal{T}^s$ from which one can deduce semi-analytic expressions for asymptotic behavior (long wavelength, increasing stack size, etc.) as well as the reflection matrix of semi-infinite woodpiles, although we will not say more about this here (see, e.g., [14,25]).

A. Grating Field Expressions

Consider an up–down symmetric grating, as in Fig. 2(a), that is embedded in a background medium of refractive index $n_b=\sqrt{\varepsilon_b\mu_b}$, with permittivity ε_b and permeability μ_b. We first specify a plane wave incident from above and having wave vector $\mathbf{k}=(\alpha_0,\beta_0,-\gamma_0)$ and polarization angle δ as defined in Fig. 2(b). The periodicity of the woodpile in x and y directions gives rise to a family of diffracted plane waves whose x and y dependencies are given by $\exp(i\alpha_p x)$ and $\exp(i\beta_q x)$ respectively, where $\alpha_p=\alpha_0+2\pi p/D$ and $\beta_q=\beta_0+2\pi q/D$ for $p,q\in\mathbb{Z}$ (while here we have used a common period D, it is not a limitation of the method). Each pair (p,q) thus specifies a diffracted plane-wave order and, for notational convenience, we map each (p,q) to a unique integer s and use the subscript s to denote quantities associated with the $(p,q)^{\text{th}}$ order. Note that the s^{th} plane-wave order is propagating if

$$\gamma_s^2=(kn_b)^2-(\alpha_p^2+\beta_q^2) \tag{1}$$

is positive and is evanescent if γ_s^2 is negative, where $k=2\pi/\lambda$ is the free-space wavenumber. The fields may thus be expressed as a superposition of these diffracted plane-wave orders, which in turn are further decomposed into *TE* and *TM* polarized resolutes. We adopt the notation used in [25], where any field expanded in such a way is represented using partitioned vectors of the form $\mathcal{F}^{\pm}=[[E_s^{\pm}]^T\,[F_s^{\pm}]^T]^T$, where $E_s^{\pm}$ and $F_s^{\pm}$ are the coefficients of the *TE* and *TM* components of the s^{th} order and where + and − denote fields propagating upwards and downwards respectively. In particular, let

$$\mathcal{F}_I^{\pm}=\begin{bmatrix}[E_{I,s}^{\pm}]\\ [F_{I,s}^{\pm}]\end{bmatrix} \quad\text{and}\quad \mathcal{F}_D^{\pm}=\begin{bmatrix}[E_{D,s}^{\pm}]\\ [F_{D,s}^{\pm}]\end{bmatrix} \tag{2}$$

represent the incoming and diffracted fields incident to the grating [see Fig. 3(a)]. The transverse components, i.e., lying in the xy plane, of the electric and magnetic fields above the grating are then

$$\mathbf{E}_t=(\mu_b/\varepsilon_b)^{1/4}\sum_s \xi_s^{1/2}[E_{I,s}^- e^{-i\gamma_s z}+E_{D,s}^+ e^{i\gamma_s z}]e^{i(\alpha_p x+\beta_q y)}\mathbf{R}_s^E + \xi_s^{1/2}[F_{I,s}^- e^{-i\gamma_s z}+F_{D,s}^+ e^{i\gamma_s z}]e^{i(\alpha_p x+\beta_q y)}\mathbf{R}_s^M, \tag{3}$$

$$\hat{\mathbf{z}}\times\mathbf{H}_t=(\varepsilon_b/\mu_b)^{1/4}\sum_s \xi_s^{1/2}[E_{I,s}^- e^{-i\gamma_s z}-E_{D,s}^+ e^{i\gamma_s z}]e^{i(\alpha_p x+\beta_q y)}\mathbf{R}_s^E + \xi_s^{-1/2}[F_{I,s}^- e^{-i\gamma_s z}-F_{D,s}^+ e^{i\gamma_s z}]e^{i(\alpha_p x+\beta_q y)}\mathbf{R}_s^M, \tag{4}$$

with $\xi_s=\gamma_s/(kn_b)$ and where $\mathbf{R}_s^E=(-\beta_q\hat{\mathbf{x}}+\alpha_p\hat{\mathbf{y}})/(\alpha_p^2+\beta_q^2)^{1/2}$ and $\mathbf{R}_s^M=(\alpha_p\hat{\mathbf{x}}+\beta_q\hat{\mathbf{y}})/(\alpha_p^2+\beta_q^2)^{1/2}$ are the *TE* and *TM* directions determined by the s^{th} diffracted order, respectively. Analogous expressions, involving $\mathcal{F}_I^+$ and $\mathcal{F}_D^-$, also hold for the fields below the grating. In the above, H is the normalized field obtained by multiplying the magnetic field by the free-space impedance $Z_0=\sqrt{\mu_0/\varepsilon_0}$.

If $\mathcal{R}_a$ and $\mathcal{R}_b$ are the reflection matrices governing the fields incident to the top and bottom surfaces of the grating, respectively, as in Fig. 3(a), and $\mathcal{T}_a$ and $\mathcal{T}_b$ are the corresponding transmission matrices, then by definition, the diffracted fields are related to the incoming fields by

$$\begin{bmatrix}\mathcal{F}_D^-\\ \mathcal{F}_D^+\end{bmatrix}=\begin{bmatrix}\mathcal{T}_a & \mathcal{R}_b\\ \mathcal{R}_a & \mathcal{T}_b\end{bmatrix}\begin{bmatrix}\mathcal{F}_I^-\\ \mathcal{F}_I^+\end{bmatrix}. \tag{5}$$

Fixing the value of p and then projecting the problem onto the yz plane allows one to use the multipole method to solve for the part of the diffracted field having an x dependence of $\exp(i\alpha_p x)$. Let $\mathbf{k}_\perp=(\beta_q,\gamma_s)$ be the projection of the

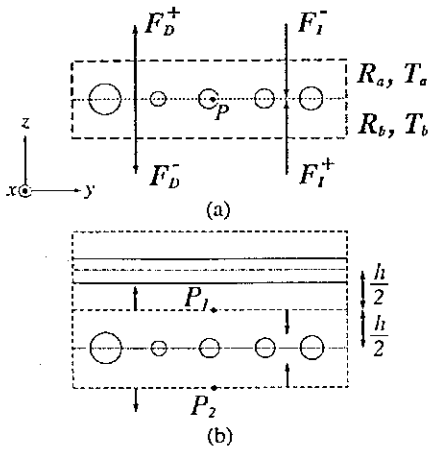

Fig. 3. (a) Incoming and diffracted fields, with phase origin at P, as well as the reflection and transmission matrices associated with the fields above and below the unit cell. (b) The unit cell with phase origins P_1 and P_2 adjusted to give the grating a total thickness of h.

wave vector onto the yz plane so that $k_\perp^2=(kn_b)^2-\alpha_p^2$ is the wavenumber of the projection. The fields at a point $\mathbf{r}=(y,z)$ inside the region A exterior to the cylinders and bounded by U^+ and U^- [see Fig. 2(a)] then satisfy the Helmholtz equation

$$[\nabla^2+k_\perp^2]V(\mathbf{r})=0 \tag{6}$$

for $V=E_x$ and $V=H_x$. Consequently by Green's theorem

$$V(\mathbf{r})=\int_A [V(\mathbf{r}')\nabla_{\mathbf{r}'}^2 G(\mathbf{r}-\mathbf{r}')-G(\mathbf{r}-\mathbf{r}')\nabla_{\mathbf{r}'}^2 V(\mathbf{r}')]d\mathbf{r}', \tag{7}$$

$$=\oint_{\partial C}\left[V(\mathbf{r}')\frac{\partial}{\partial n'}G(\mathbf{r}-\mathbf{r}')-G(\mathbf{r}-\mathbf{r}')\frac{\partial}{\partial n'}V(\mathbf{r}')\right]d\mathbf{r}', \tag{8}$$

where $\partial C=U^+\cup U^-\cup_{j=1}^{N_c}C_j$, with C_j denoting the boundary of cylinder j, and where the associated Green's function G satisfies

$$[\nabla^2+k_\perp^2]G(\mathbf{r})=\sum_{n=-\infty}^{\infty}\delta(\mathbf{r}-nD\hat{\mathbf{y}})\exp(i\beta_0 nD). \tag{9}$$

In the above, the phase factors $\exp(i\beta_0 nD)$ match the quasi-periodicity of the fields in the direction of the grating [the relevant forms of G are given by Eqs. (A1) and (A2)]. The evaluation of Eq. (8) also requires the following local representation of the fields in the vicinity of cylinder l:

$$V_l(\mathbf{r}_l)=\sum_{n=-\infty}^{\infty}[A_n^{l,V}J_n(k_\perp r_l)+B_n^{l,V}H_n(k_\perp r_l)]e^{in\theta_{r_l}}e^{i\alpha_p x}. \tag{10}$$

Here and elsewhere, J_n and H_n denote Bessel functions and Hankel functions of the first kind. Substituting Eqs. (A1), (A2), and (10) into Eq. (8) we arrive at the Wijngaard expansion

$$\begin{aligned}V_l(\mathbf{r}_l)=&\sum_{n=-\infty}^{\infty}B_n^{l,V}H_n(k_\perp r_l)e^{in\theta_{r_l}}e^{i\alpha_p x}\\&+\sum_{n=-\infty}^{\infty}J_n(k_\perp r_l)e^{in\theta_{r_l}}e^{i\alpha_p x}\left[\sum_{j=1}^{N_c}\sum_{m=-\infty}^{\infty}B_m^{j,V}S_{n-m}^{lj}\right.\\&\left.+\sum_{q=-\infty}^{\infty}(J_{nq}^{l,-}\delta_q^{-,V}+J_{nq}^{l,+}\delta_q^{+,V})\right],\end{aligned} \tag{11}$$

where S_{n-m}^{lj}, $l\neq j$ are the local lattice sums [26] and, for simplicity, we define $S_m=S_m^{ll}$ to be the global lattice sums [see Eqs. (A3) and (A4)], for which a stable and efficient means of evaluation is essential [27]. Here, $\delta_q^{\pm,V}$ are the longitudinal components of the incoming fields, while $J_{nq}^{l,\pm}=(\pm 1)^n\exp[\pm in\arg(\gamma_s+i\beta_q)]\exp(i\beta_q c_l)$ change the basis of the incident field from plane waves to multipoles. The two representations of the local field, Eqs. (10) and (11), allow us to express the incoming multipole coefficients in terms of the outgoing coefficients so that, using matrix notation,

$$\mathcal{A}=\mathcal{S}\mathcal{B}+\mathcal{J}\mathcal{D}^-+\mathcal{J}^+\mathcal{D}^+. \tag{12}$$

Equation (12) is known as the Rayleigh identity, in which

$$\mathcal{A}=\begin{bmatrix}[\mathsf{A}^{l,E}]\\[\mathsf{A}^{l,H}]\end{bmatrix}, \tag{13}$$

$\mathsf{A}^{l,E/H}=[A_n^{l,E/H}]$ ($\mathcal{B}$ is defined analogously to $\mathcal{A}$), $\mathcal{S}\mathcal{B}$ represents the scattered fields sourced by each cylinder, and $\mathcal{J}\mathcal{D}^-$ ($\mathcal{J}^+\mathcal{D}^+$) is the multipole representation of the incoming field from above (below). See Appendix A for details.

The fields inside cylinder l can also be expressed in terms of cylindrical harmonics; specifically, if n_l is the refractive index of cylinder l, then for $\mathbf{r}_l$ inside C_l there exist coefficients $C_n^{l,V}$ such that

$$V_l(\mathbf{r}_l)=\sum_{n=-\infty}^{\infty}C_n^{l,V}J_n(k_{\perp,l}r_l)e^{in\theta_{r_l}}e^{i\alpha_p x}, \tag{14}$$

with $k_{\perp,l}^2=(kn_l)^2-\alpha_p^2$. By using Eqs. (10) and (14) and also imposing the condition that the tangential components E_θ, H_θ, E_x, and E_x be continuous across the cylinder boundaries, one finds a second equation relating $\mathcal{A}$ to $\mathcal{B}$:

$$\mathcal{A}=-\mathcal{M}\mathcal{B}. \tag{15}$$

The matrix $\mathcal{M}$ encapsulates the material properties of the cylinders. It should be noted that in general $\mathcal{M}$ is not diagonal, hence Eq. (15) has the effect of coupling the electric and magnetic problems (see Appendix B for the expressions for $\mathcal{M}$). Combining Eqs. (12) and (15), we have for the outgoing multipole coefficients

$$\mathcal{B}=-(\mathcal{M}+\mathcal{S})^{-1}\mathcal{J}\mathcal{D}, \tag{16}$$

where $\mathcal{J}=[\mathcal{J}^-\ \mathcal{J}^+]$, and $\mathcal{D}=[(\mathcal{D}^-)^T\ (\mathcal{D}^+)^T]^T$. Equation (16) can be used to calculate the fields incident to the grating and, hence, the reflection and transmission matrices.

B. Scattering Matrices for a Grating

The diffracted fields appearing in Eq. (5) can be recovered by again evaluating Eq. (8), this time taking $\mathbf{r}$ to lie above and below the cylinders in turn; thus, the diffracted fields will be expressed in terms of the outgoing multipole coefficients $\mathcal{B}$ of Eq. (16). The longitudinal components of diffracted fields are found to be [26]

$$\mathcal{F}=\mathcal{D}+\frac{2}{D}\mathcal{G}\mathcal{K}\mathcal{B}, \tag{17}$$

where $\mathcal{K}$ reverts back to the plane-wave basis from the multipole basis and is defined analogously to $\mathcal{J}$ [see Eq. (A5)]. Equation (17) includes a prefactor $\mathcal{G}$ that serves to normalize the reflected and transmitted energy (the particulars are omitted, as $\mathcal{G}$ does not appear in the final expressions for the scattering matrices). From Eqs. (16) and (17) one can derive

$$\begin{bmatrix}\mathcal{F}_D^-\\\mathcal{F}_D^+\end{bmatrix}=\left[\mathcal{I}-\frac{2}{D}\hat{\mathcal{X}}^{-1}\mathcal{Z}^{-1}\mathcal{G}\mathcal{K}(\mathcal{M}+\mathcal{S})^{-1}\mathcal{J}\mathcal{Z}\hat{\mathcal{X}}\right]\begin{bmatrix}\mathcal{F}_I^-\\\mathcal{F}_I^+\end{bmatrix}, \tag{18}$$

[Cf. Eq. (5)]. The multipole scattering operator $\mathcal{K}(\mathcal{M}+\mathcal{S})^{-1}\mathcal{J}$ acts on the longitudinal components of the fields;

however, the scattering matrices defined in Eq. (5) are formulated to act on plane-wave diffraction orders that have been resolved into *TE* and *TM* components. Therefore a change of coordinate systems, which is achieved by the term $\mathcal{Z}\hat{\mathcal{X}}$, is first necessary (see Appendix A).

The single-layer scattering matrices are inferred by identifying the coefficient matrix in Eq. (18) with that in Eq. (5); however, in the case of up–down symmetric gratings, the size of the multipole scattering operator can be halved using a folding procedure. We proceed by rewriting Eq. (18) in terms of symmetric and antisymmetric quantities (denoted using the superscripts s and a) to give

$$\begin{bmatrix} \mathcal{F}_D \\ \mathcal{F}_D^+ \end{bmatrix} = \begin{bmatrix} \mathcal{F}_I \\ \mathcal{F}_I^+ \end{bmatrix} - \frac{kn_b}{k_\perp{}^2 D}\mathcal{T}^{-1}\mathcal{X}\mathcal{Z}^{-1}\begin{bmatrix} \mathcal{K}^s\mathcal{L}\mathcal{J}^s & \mathcal{K}^s\mathcal{L}\mathcal{J}^a \\ \mathcal{K}^a\mathcal{L}\mathcal{J}^s & \mathcal{K}^a\mathcal{L}\mathcal{J}^a \end{bmatrix}\mathcal{Z}\mathcal{X}\mathcal{T}\begin{bmatrix} \mathcal{F}_I \\ \mathcal{F}_I^+ \end{bmatrix}, \tag{19}$$

(Cf. Eq. (52) of [25]) where

$$\mathcal{T} = \begin{bmatrix} \mathsf{I} & \mathsf{I} \\ \mathsf{I} & -\mathsf{I} \end{bmatrix}, \tag{20}$$

$\mathcal{L}=(\mathcal{M}+\mathcal{S})^{-1}$. It can be shown that $\mathcal{K}^s\mathcal{L}\mathcal{J}^a$ and $\mathcal{K}^a\mathcal{L}\mathcal{J}^s$ vanish for up–down symmetric gratings, while for $\mathcal{K}^s\mathcal{L}\mathcal{J}^s$ and $\mathcal{K}^a\mathcal{L}\mathcal{J}^a$ the rows that correspond to the negative multipole orders are redundant, which then allows one to truncate $\mathcal{K}^{a/s}$, $\mathcal{J}^{a/s}$ and $\mathcal{L}$ by only retaining the rows and columns for the multipole orders $n,m\geq 0$. Using a tilde to denote such a truncated matrix, the scattering matrices for an up–down symmetric grating are then

$$\mathcal{R}_a = \mathcal{R}_b = -\frac{kn_b}{2k_\perp^2 D}\mathsf{X}\mathsf{Z}^{-1}(\tilde{\mathcal{K}}^s\varepsilon^s\tilde{\mathcal{L}}^s\bar{\mathcal{J}}^s - \bar{\mathcal{K}}^a\varepsilon^a\bar{\mathcal{L}}^a\tilde{\mathcal{J}}^a)\mathsf{Z}\mathsf{X}, \tag{21}$$

and

$$\mathcal{T}_a = \mathcal{T}_b = \mathcal{I} - \frac{kn_b}{2k_\perp^2 D}\mathsf{X}\mathsf{Z}^{-1}(\tilde{\mathcal{K}}^s\varepsilon^s\tilde{\mathcal{L}}^s\bar{\mathcal{J}}^s + \bar{\mathcal{K}}^a\varepsilon^a\bar{\mathcal{L}}^a\tilde{\mathcal{J}}^a)\mathsf{Z}\mathsf{X}. \tag{22}$$

The definitions of the terms on the right-hand sides of Eqs. (21) and (22) are provided in Appendix A.

C. Woodpile Scattering Matrices

Recall that the scattering matrices just derived are 2D in that p is fixed, i.e., they act on fields having an assumed x dependency of $\exp(i\alpha_p x)$. If each of the fields $\mathcal{F}$ in Eq. (5) are ordered so that

$$\mathcal{F} = [\cdots\ \mathsf{F}_{-1}^T\ \mathsf{F}_0^T\ \mathsf{F}_1^T\ \cdots]^T, \tag{23}$$

with $\mathsf{F}_p=[f_{(p,q)}]$, then the reflection matrix for a single layer of a woodpile at conical incidence is $\mathcal{R}=\mathrm{diag}[\mathcal{R}_p]$, where $\mathcal{R}_p$ is a 2D reflection matrix (and similarly for $\mathcal{T}$). To find the scattering matrices for a y aligned grating, a rotated coordinate system (x',y',z') must be used, namely $x'=y$, $y'=-x$, $z'=z$, and hence $\alpha'_p=\beta_p$, $\beta'_q=-\alpha_{-q}$ and $\gamma'_{(p,q)}=\gamma_{(-q,p)}$. We see that in general the channels $s'=(p,q)'$ and $s=(p,q)$ do not correspond to the same plane-wave order since $(p,q)'$ maps to $(-q,p)$, so, assuming that the channel order is given by Eq. (23), the entries of the scattering matrices for the rotated system must be permuted accordingly.

Recurrence relationships for the scattering matrices for a stack of $(s+1)$ non-interpenetrating gratings are then readily found from Eqs. (21) and (22) by expressing the fields incident to the s and $(s+1)^{\text{th}}$ layers in terms of $\mathcal{R}$ and $\mathcal{T}$ of the $(s+1)^{\text{th}}$ layer and $\mathcal{R}^s$ and $\mathcal{T}^s$ of the s layer stack beneath. We merely state the results (a full derivation may be found in [14]):

$$\mathcal{R}_a^{s+1} = \tilde{\mathcal{R}}_a + \tilde{\mathcal{T}}_b\mathcal{R}_a^s(\mathcal{I}-\tilde{\mathcal{R}}_b\mathcal{R}_a^s)^{-1}\tilde{\mathcal{T}}_a, \tag{24}$$

$$\mathcal{T}_a^{s+1} = \mathcal{T}_a^s(\mathcal{I}-\tilde{\mathcal{R}}_b\mathcal{R}_a^s)^{-1}\tilde{\mathcal{T}}_a, \tag{25}$$

$$\mathcal{R}_b^{s+1} = \mathcal{R}_b^s + \mathcal{T}_a^s\tilde{\mathcal{R}}_b(\mathcal{I}-\mathcal{R}_a^s\tilde{\mathcal{R}}_b)^{-1}\mathcal{T}_b^s, \tag{26}$$

$$\mathcal{T}_b^{s+1} = \tilde{\mathcal{T}}_b(\mathcal{I}-\mathcal{R}_a^s\tilde{\mathcal{R}}_b)^{-1}\mathcal{T}_b^s. \tag{27}$$

Here, the change in phase that occurs for fields propagating between successive layers has been incorporated into $\tilde{\mathcal{R}}_{a/b}$ and $\tilde{\mathcal{T}}_{a/b}$ by applying a padding $\mathcal{P}$ symmetrically above and below the layer. This gives the grating an artificial thickness h equal to the distance between adjacent layers [see Fig. 3(b)]. In addition, it is usual to interleave the layers; hence, for a stack consisting of a finite number of grating pairs, a lateral shift transform $\mathcal{Q}$ that effects a shift of $d/2$ (with d as in Fig. 1) in both the x and y directions is applied to the gratings of every second pair:

$$\begin{bmatrix} \tilde{\mathcal{R}}_a & \tilde{\mathcal{T}}_b \\ \tilde{\mathcal{T}}_a & \tilde{\mathcal{R}}_b \end{bmatrix} = \begin{bmatrix} \mathcal{Q}\mathcal{P} & 0 \\ 0 & \mathcal{Q}\mathcal{P} \end{bmatrix}\begin{bmatrix} \mathcal{R}_a & \mathcal{T}_b \\ \mathcal{T}_a & \mathcal{R}_b \end{bmatrix}\begin{bmatrix} \mathcal{P}\mathcal{Q}^{-1} & 0 \\ 0 & \mathcal{P}\mathcal{Q}^{-1} \end{bmatrix}, \tag{28}$$

where $\mathcal{P}=\mathrm{diag}[\mathsf{P}\ \mathsf{P}]$, $\mathsf{P}=\mathrm{diag}[e^{i\gamma_s h/2}]$, $\mathcal{Q}=\mathrm{diag}[\mathsf{Q}\ \mathsf{Q}]$ and

$$\mathsf{Q} = \begin{cases} \mathrm{diag}[e^{i(\alpha_p+\beta_q)d/2}], & \text{for a shifted layer,} \\ \mathsf{I}, & \text{otherwise.} \end{cases} \tag{29}$$

D. Band Structure

The band structure of a woodpile can be readily computed from knowledge of the Bloch modes. For the Bloch analysis, an orthogonal grating pair is used as the stacking unit, with $\mathcal{R}_{a/b}^{(2)}$ and $\mathcal{T}_{a/b}^{(2)}$ for the pair computed from the recurrences of Eq. (24). Consequently, as the Bloch method is only applicable to infinite stacks, the phase origins of the fields incident to the pair must be offset in order to effect an interleaving of the structure, as in Fig. 4(a). This is achieved by redefining $\mathsf{Q}=\mathrm{diag}[e^{i(\alpha_p+\beta_q)d/4}]$ in Eq. (29) so that applying the transform $\mathcal{Q}$ to the scattering matrices results in a lateral shear of the lattice:

$$\begin{bmatrix} \tilde{\mathcal{R}}_a^{(2)} & \tilde{\mathcal{T}}_b^{(2)} \\ \tilde{\mathcal{T}}_a^{(2)} & \tilde{\mathcal{R}}_b^{(2)} \end{bmatrix} = \begin{bmatrix} \mathcal{Q} & 0 \\ 0 & \mathcal{Q}^{-1} \end{bmatrix}\begin{bmatrix} \mathcal{R}_a^{(2)} & \mathcal{T}_b^{(2)} \\ \mathcal{T}_a^{(2)} & \mathcal{R}_b^{(2)} \end{bmatrix}\begin{bmatrix} \mathcal{Q}^{-1} & 0 \\ 0 & \mathcal{Q} \end{bmatrix}. \tag{30}$$

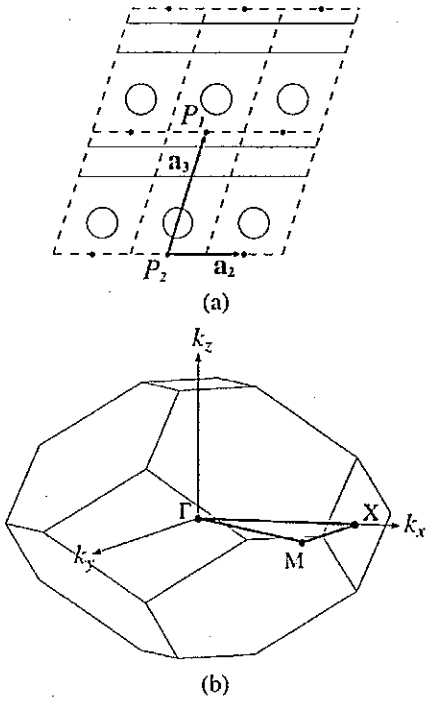

Fig. 4. (a) For the Bloch analysis, a pair of orthogonal rods constitutes a single point of a body-centered tetragonal (BCT) lattice for which the primitive vectors are $\mathbf{a}_1=d\hat{\mathbf{x}}$ (not shown), $\mathbf{a}_2=d\hat{\mathbf{y}}$, and $\mathbf{a}_3=(d/2)\hat{\mathbf{x}}+(d/2)\hat{\mathbf{y}}+2h\hat{\mathbf{z}}$. Offsetting the phase origins P_1 and P_2 laterally, as indicated above, has the effect of interleaving the layers of an infinite stack. (b) The boundaries of the first Brillouin zone (thin lines) and the SBZ (thick lines) of a prolate BCT lattice, such as the lattice shown in part (a).

If $\mathcal{F}_1=[(\mathcal{F}_1^-)^T(\mathcal{F}_1^+)^T]^T$ and $\mathcal{F}_2=[(\mathcal{F}_2^-)^T(\mathcal{F}_2^+)^T]^T$ are the Bloch modes at the top and bottom surfaces of a constituent grating pair, respectively, then Bloch's theorem requires that

$$\mathcal{F}_2=\mu\mathcal{F}_1, \tag{31}$$

where $\mu=\exp(-i\mathbf{k}\cdot\mathbf{a}_3)$, $\mathbf{k}=(k_x,k_y,k_z)$ is the Bloch vector, and $\mathbf{a}_3$ is the lattice replication vector in the stacking direction [see Fig. 4(a)]. Bloch's theorem can be recast as an eigenvalue problem for the inter-layer transfer matrix $\mathfrak{T}$, which propagates the fields across the pair (i.e., $\mathfrak{T}\mathcal{F}_1=\mathcal{F}_2$) and is constructed from the reflection and transmission matrices of a pair of orthogonal gratings:

$$\mathfrak{T}\mathcal{F}_1=\mu\mathcal{F}_1. \tag{32}$$

In practice, however, one does not solve the above eigenvalue problem but instead computes the eigenvalues of a derived form of Eq. (32) that is more numerically robust (see, eg., [25,28]). It is clear from Eq. (32) that modes for which $|\mu|\neq 1$ are evanescent modes, while for propagating modes $|\mu|=1$. Since the transfer matrix is expressed solely in terms of $\tilde{\mathcal{R}}_{a/b}^{(2)}$ and $\tilde{\mathcal{T}}_{a/b}^{+2)}$, Eq. (32) can be regarded as a function that determines the set of all k_zs for which Bloch states exist for a given k_x, k_y, and wavenumber k. Thus to compute the band structure, it suffices to use Eq. (32) to recover the propagating modes for each distinct $\mathbf{k}_t=(k_x,k_y)$ along the boundary of the surface Brillouin zone (SBZ) [29] [shown in Fig. 4(b)]. This procedure was used to compute the band diagram in Fig. 5.

3. APPLICATIONS

We used the above techniques to model two types of waveguides based on the woodpile geometry. In keeping with the notation established in Section 2.D, $\mathbf{k}=(k_x,k_y,k_z)$ specifies the wave vector of the incoming field. In both cases, a waveguide is created by changing the size of selected cylinders of the 15th layer of a 28 layer chalcogenide glass woodpile, where the bottom layer is taken to be the first layer. The radii and refractive index of the cylinders are $r=0.15d$ and $n_l=2.68$, respectively (the refractive indices of chalcogenide glass typically lie between 2 and 3), where d is the pitch of the constituent gratings (as in Fig. 1). The background refractive index is air ($n_b=1$), and thus the inter-layer spacing for the layers comprising the bulk must be chosen so that adjacent layers abut. Here, a spacing of $h=0.3002d$ is used.

Using the method outlined in Section 2.D, the infinite woodpile was found to have a complete PBG spanning $0.50\leq kd/(2\pi)\leq 0.52$, i.e., for wavelengths $1.9\leq\lambda/d\leq 2.0$ (see Fig. 5). About 28 layers are needed in order to observe a profound drop in the transmittance over these frequencies for k_x values along the $\Gamma-X$ path of the reciprocal lattice, with $k_y=0$ fixed [recall that k_z, or equivalently γ_0, changes implicitly according to Eq. (1)]. The existence of waveguide modes is inferred from the transmission spectra for both *TE* and *TM* polarization, i.e., for an incident field with $E_x=E_z=H_y=0$ and $E_y=H_x=H_z=0$, respectively. It should be noted that while the singular behavior near the contact points of the rods was found to give the fields a strongly '*TM*-like' character at resonant wavelengths in that the magnitude of E_z was much greater than those of E_x, E_y, H_x, H_y, and H_z, the fields at these points are not expected to contribute significantly to the waveguiding ability of the defect layer.

If $s=0$ specifies the specular channel, i.e., $p=q=0$, then the incoming field $\mathcal{D}=[[D_s^{E,-}]^T[D_s^{H,-}]^T]^T$ incident to the top surface of the woodpile is determined by the polarization angle δ according to

$$D_s^{E,-}=\delta_{s0}\cos\delta \tag{33}$$

and

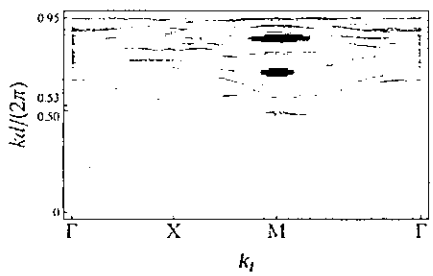

Fig. 5. Plot of the number of propagating Bloch modes for each (normalized) k as the in-plane Bloch vector $\mathbf{k}_t=(k_x,k_y)$ traverses the boundary of the SBZ. White indicates the absence of propagating states. The structural parameters of the woodpile are given in Section 3.

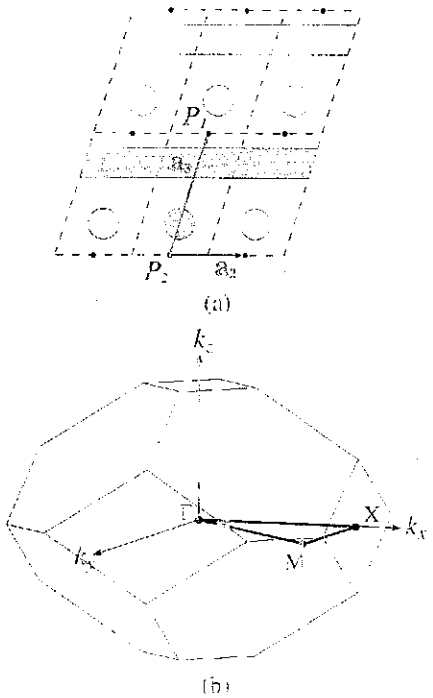

Fig. 4. (a) For the Bloch analysis, a pair of orthogonal rods constitutes a single point of a body-centered tetragonal (BCT) lattice for which the primitive vectors are $\mathbf{a}_1=d\hat{\mathbf{x}}$ (not shown), $\mathbf{a}_2=d\hat{\mathbf{y}}$, and $\mathbf{a}_3=(d/2)\hat{\mathbf{x}}+(d/2)\hat{\mathbf{y}}+2h\hat{\mathbf{z}}$. Offsetting the phase origins P_1 and P_2 laterally, as indicated above, has the effect of interleaving the layers of an infinite stack. (b) The boundaries of the first Brillouin zone (thin lines) and the SBZ (thick lines) of a prolate BCT lattice, such as the lattice shown in part (a).

If $\mathcal{F}_1=[(\mathcal{F}_1^+)^T(\mathcal{F}_1^-)^T]^T$ and $\mathcal{F}_2=[(\mathcal{F}_2^+)^T(\mathcal{F}_2^-)^T]^T$ are the Bloch modes at the top and bottom surfaces of a constituent grating pair, respectively, then Bloch's theorem requires that

$$\mathcal{F}_2=\mu\mathcal{F}_1, \tag{31}$$

where $\mu=\exp(-i\mathbf{k}\cdot\mathbf{a}_3)$, $\mathbf{k}=(k_x,k_y,k_z)$ is the Bloch vector, and $\mathbf{a}_3$ is the lattice replication vector in the stacking direction (see Fig. 4(a)). Bloch's theorem can be recast as an eigenvalue problem for the inter-layer transfer matrix $\mathfrak{T}$, which propagates the fields across the pair (i.e., $\mathfrak{T}\mathcal{F}_1=\mathcal{F}_2$) and is constructed from the reflection and transmission matrices of a pair of orthogonal gratings:

$$\mathfrak{T}\mathcal{F}_1=\mu\mathcal{F}_1. \tag{32}$$

In practice, however, one does not solve the above eigenvalue problem but instead computes the eigenvalues of a derived form of Eq. (32) that is more numerically robust (see, e.g., [25,28]). It is clear from Eq. (32) that modes for which $|\mu|\neq 1$ are evanescent modes, while for propagating modes $|\mu|=1$. Since the transfer matrix is expressed solely in terms of $\tilde{\mathcal{R}}_{a/b}^{(2)}$ and $\tilde{\mathcal{T}}_{a/b}^{(2)}$, Eq. (32) can be regarded as a function that determines the set of all k_zs for which Bloch states exist for a given k_x, k_y, and wavenumber k. Thus to compute the band structure, it suffices to use Eq. (32) to recover the propagating modes for each distinct $\kappa_t=(k_x,k_y)$ along the boundary of the surface Brillouin zone (SBZ) [29] [shown in Fig. 4(b)]. This procedure was used to compute the band diagram in Fig. 5.

3. APPLICATIONS

We used the above techniques to model two types of waveguides based on the woodpile geometry. In keeping with the notation established in Section 2.D, $\mathbf{k}=(k_x,k_y,k_z)$ specifies the wave vector of the incoming field. In both cases, a waveguide is created by changing the size of selected cylinders of the 15th layer of a 28 layer chalcogenide glass woodpile, where the bottom layer is taken to be the first layer. The radii and refractive index of the cylinders are $r=0.15d$ and $n_1=2.68$, respectively (the refractive indices of chalcogenide glass typically lie between 2 and 3), where d is the pitch of the constituent gratings (as in Fig. 1). The background refractive index is air ($n_0=1$), and thus the inter-layer spacing for the layers comprising the bulk must be chosen so that adjacent layers abut. Here, a spacing of $h=0.3002d$ is used.

Using the method outlined in Section 2.D, the infinite woodpile was found to have a complete PBG spanning $0.50\leq kd/(2\pi)\leq 0.52$, i.e., for wavelengths $1.9\leq\lambda/d\leq 2.0$ (see Fig. 5). About 28 layers are needed in order to observe a profound drop in the transmittance over these frequencies for k_x values along the $\Gamma-\mathrm{X}$ path of the reciprocal lattice, with $k_y=0$ fixed (recall that k_z, or equivalently γ_0, changes implicitly according to Eq. (1)). The existence of waveguide modes is inferred from the transmission spectra for both *TE* and *TM* polarization, i.e., for an incident field with $E_x=E_z=H_y=0$ and $E_y=H_x=H_z=0$, respectively. It should be noted that while the singular behavior near the contact points of the rods was found to give the fields a strongly '*TM*-like' character at resonant wavelengths in that the magnitude of E_z was much greater than those of E_x, E_y, H_x, H_y, and H_z, the fields at these points are not expected to contribute significantly to the waveguiding ability of the defect layer.

If $s=0$ specifies the specular channel, i.e., $p=q=0$, then the incoming field $\mathcal{D}=[(D_s^{E,-})^T(D_s^{H,-})^T]^T$ incident to the top surface of the woodpile is determined by the polarization angle δ according to

$$D_s^{E,-}=\delta_{s,1}\cos\delta \tag{33}$$

and

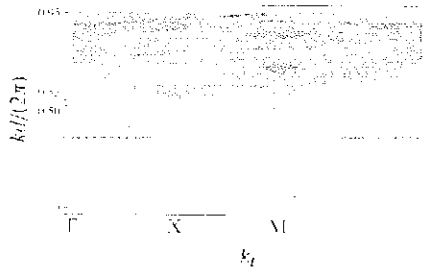

Fig. 5. Plot of the number of propagating Bloch modes for each normalized k as the in-plane Bloch vector $\kappa_t=(k_x,k_y)$ traverses the boundary of the SBZ. White indicates the absence of propagating states. The structural parameters of the woodpile are given in Section 3.

$$D_s^{II,-} = \delta_{s0} \sin \delta, \tag{34}$$

where δ_{ij} is the Kronecker delta

$$\delta_{ij} = \begin{cases} 1, & \text{for } i=j, \\ 0, & \text{otherwise.} \end{cases} \tag{35}$$

The field transmitted through to the bottom surface of the woodpile is then $\mathbf{t}=[t_s]=\mathcal{T}_a^s\mathcal{D}$, where $\mathcal{T}_a^s$ is the transmission matrix associated with the top surface of the woodpile. Similarly, the field reflected back by the top surface is $\mathbf{r}=\mathcal{R}_a^s\mathcal{D}$. The transmittance is then

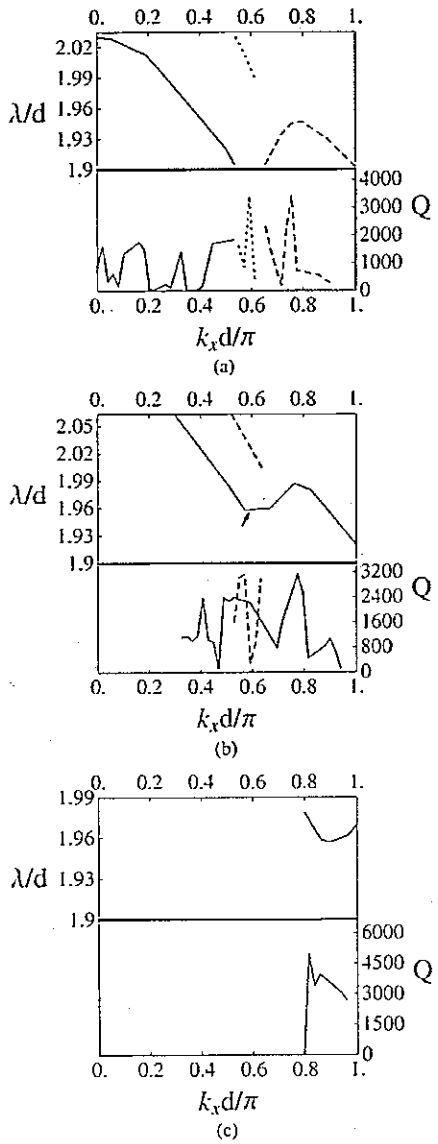

Fig. 6. (Color online) Location of transmission maxima (top) for *TM* incidence and the corresponding Q-factors (bottom) for the CROW using defect sizes of (a) $r_w=0$, (b) $r_w=0.5r$, and (c) $r_w=0.8r$ as k_x varies. The transmittance is negligible except for the resonances. As r_w increases, the resonances move to longer wavelengths. Fields at the point indicated (arrow) in part (b) are shown in Fig. 7.

$$T = \sum_s |t_s|^2, \tag{36}$$

where the sum is taken over only the propagating plane-wave orders, with reflectance R similarly defined. One test of the correctness of our implementation is that $T+R=1$ should hold for lossless materials (recall that the entries of $\mathcal{T}$ and $\mathcal{R}$ were previously normalized).

A. A Coupled-Resonator Optical Waveguide

The first waveguide we consider is one created by changing the radius r_w of every second cylinder of the defect layer; thus, for the defect layer we employ a unit cell of length $D=2d$ containing $N_c=2$ cylinders. Figure 6 shows how the transmittance varies for *TM* incidence for $r_w=0$, $r_w=0.5r$, and $r_w=0.8r$, respectively, as k_x is gradually increased. In each case, one or more strong transmission peaks sweep through frequencies corresponding to the PBG of the host woodpile (no such peaks were found for TE incidence). These arise from defect modes supported by the waveguide and are not present in the transmission spectrum of the regular woodpile. As is to be expected, the quality factors $Q=T/\Delta T$ of the resonances tend to be higher for wavelengths near the middle of the PBG, where ΔT is the FWHM. Further, the Q factors also exhibit an oscillatory dependence on k_x, as Fig. 6 shows. We expect the turning points of the trajectories of the resonances in Fig. 6 to correspond to 'slow-light' modes, i.e., having low group velocity $\partial\omega/\partial k_x$. The fields at one of the resonances are shown in Fig. 7. The fields are '*TM*-like' for the reason mentioned above, and are localized to the waveguide layer, indicative of a defect mode.

B. A Linear Waveguide

Ideally a linear waveguide would be modeled by perturbing a single cylinder in the defect layer. We have approximated this by using a unit cell of length $D=11d$ comprising 11 cylinders spaced equally along the axis of the grating (however, techniques exist [23,24] for overcoming this restriction) and by changing the radius r_w of the central cylinder of the unit cell. The length of the unit cell and the fineness of the spectral features make this approach particularly demanding. An alternative is to use an infinite number of cladding layers, which allows the defect modes to be found directly. The advantage in doing this is that it does not require high-resolution sampling of the bandgap frequencies; however, we do not use this approach here. Figures 8 and 9 show how the transmittance varies for *TM* incidence as k_x and r_w are increased, respectively. As before, the defect causes prominent resonances to appear inside the PBG, while no such resonances are present for *TE* incidence. Again, the fields were found to be strongly '*TM*-like' at the resonances. Figure 10 shows that for $r_w=0.5r$, the field at the resonance wavelength $\lambda/d=1.935$ (as identified from Fig. 9) is concentrated around the defect rod. Figure 8 suggests that the Q factors do not change dramatically for different values of k_x, thus from Fig. 9 we posit that smaller structural perturbations will create defect modes that occupy smaller volumes and thus incur fewer scattering losses as they propagate along the waveguide.

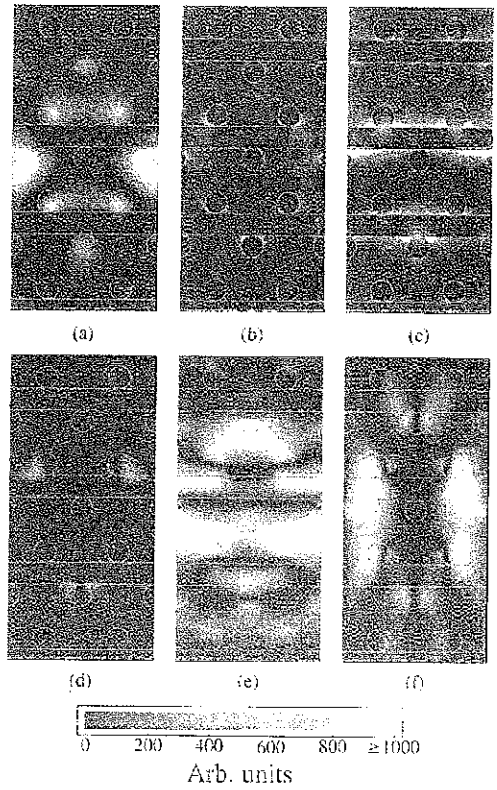

Fig. 7. (Color online) Field intensity in the vicinity of the CROW (only one period in the horizontal direction is shown): (a) $|E_x|^2$, (b) $|E_y|^2$, (c) $|E_z|^2$, (d) $|H_x|^2$, (e) $|H_y|^2$, and (f) $|H_z|^2$. The radius of the defect rods (dashed circles) is $r_a = 0.5r$, and the parameters of the incoming field are $k_x d/\pi = 0.59$, $k_y = 0$, and $\lambda/d = 1.958$, i.e., for the point indicated in Fig. 8(b).

C. Homogenization

In this section we derive explicit expressions for the scattering matrices [Eqs. (21) and (22)] in the long wavelength limit for normal incidence, i.e., $k_x = k_y = 0$, for a weakly disordered woodpile. From these, it is demonstrated that the magnitudes of the response fields are largely independent of the polarization of the incident

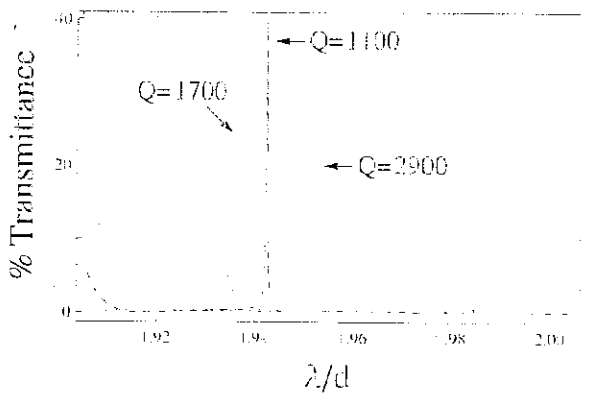

Fig. 8. (Color online) Transmittance and Q factors for a linear waveguide for TM incidence with $r_a = 0.5r$ and $k_y = 0$ fixed and $k_x d/\pi = 0.86$ (red/dotted), 0.92 (blue/dashed), and 1.00 (green/solid). The resonance shifts to shorter wavelengths as k_x increases.

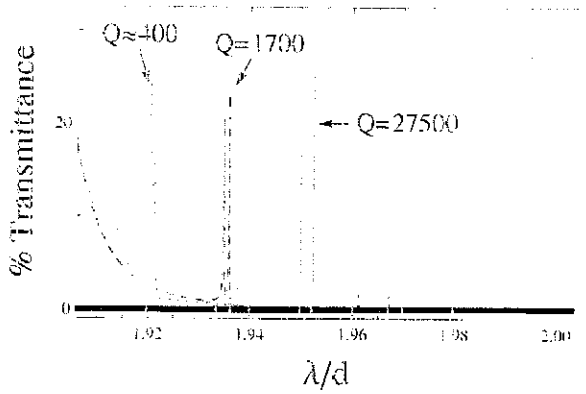

Fig. 9. (Color online) Transmittance and Q factors for a linear waveguide for TM incidence with $k_x d/\pi = 1$ and $k_y = 0$ fixed. The defect size is $r_a = 0$ (red/dotted), i.e., cylinder completely removed, $r_a = 0.5r$ (blue/dashed), $r_a = 0.8r$ (green/thin), and $r_a = r$, i.e., no defect (black/thick). The resonances shift to longer wavelengths as r_a increases.

field and that the woodpile behaves as though it were a uniform medium (details are given in Appendix C).

Initially consider a grating aligned parallel to the x axis. For normal incidence $\mathbb{M}^{EH} = \mathbb{M}^{HE} = 0$, consequently the electric and magnetic problems decouple. Further, when $\lambda \gg D$ only the specular order $s = (0,0)$ is required so

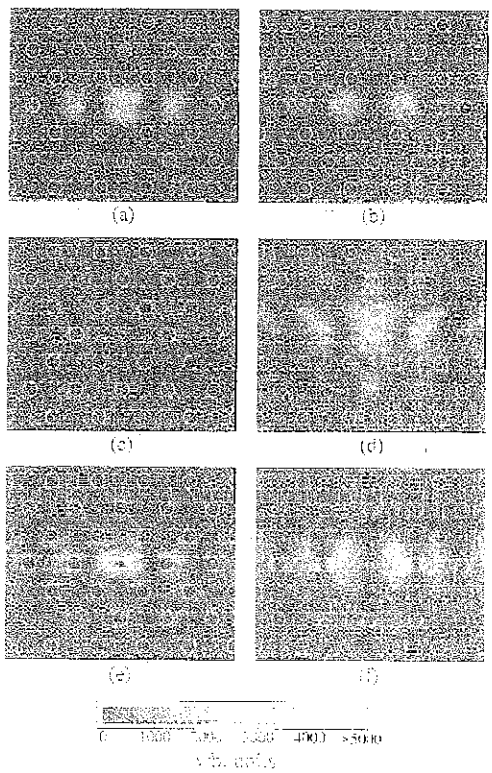

Fig. 10. (Color online) Field intensity in the vicinity of one linear waveguide: (a) $|E_x|^2$, (b) $|E_y|^2$, (c) $|E_z|^2$, (d) $|H_x|^2$, (e) $|H_y|^2$, and (f) $|H_z|^2$. The radius of the defect rod (dashed circle) is $r_a = 0.5r$, and the parameters of the incident field are $k_x \pi/d = 1$, $k_y = 0$, and $\lambda/d = 1.936$, i.e., for the resonance indicated in Fig. 9. An animation showing $|E_y|^2$ for the entire unit cell is available online.

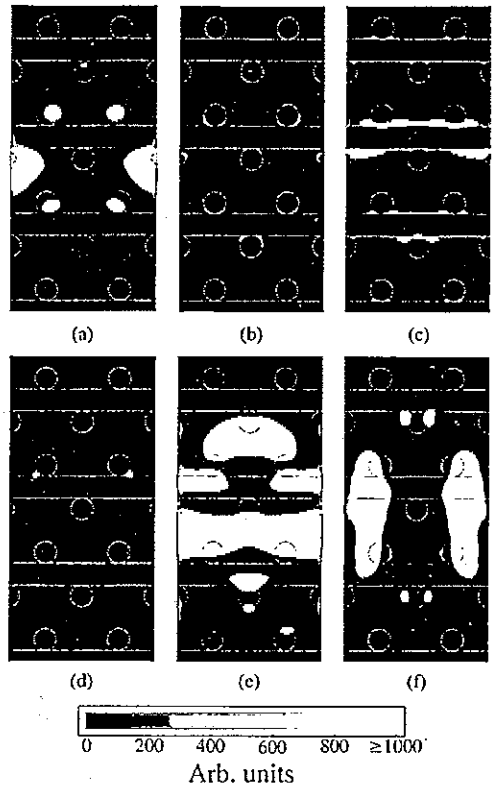

Fig. 7. (Color online) Field intensity in the vicinity of the CROW (only one period in the horizontal direction is shown): (a) $|E_x|^2$, (b) $|E_y|^2$, (c) $|E_z|^2$, (d) $|H_x|^2$, (e) $|H_y|^2$, and (f) $|H_z|^2$. The radius of the defect rods (dashed circles) is $r_w=0.5r$, and the parameters of the incoming field are $k_x d/\pi=0.59$, $k_y=0$, and $\lambda/d=1.958$, i.e., for the point indicated in Fig. 6(b).

C. Homogenization

In this section we derive explicit expressions for the scattering matrices [Eqs. (21) and (22)] in the long wavelength limit for normal incidence, i.e., $k_x=k_y=0$, for a weakly disordered woodpile. From these, it is demonstrated that the magnitudes of the response fields are largely independent of the polarization of the incident

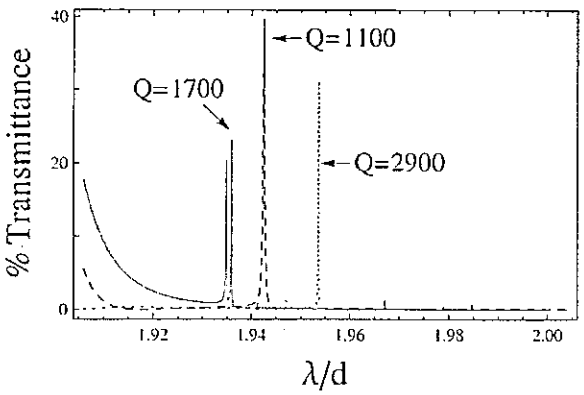

Fig. 8. (Color online) Transmittance and Q factors for a linear waveguide for TM incidence with $r_w=0.5r$ and $k_y=0$ fixed and $k_x d/\pi=0.86$ (red/dotted), 0.92 (blue/dashed), and 1.0 (green/solid). The resonance shifts to shorter wavelengths as k_x increases.

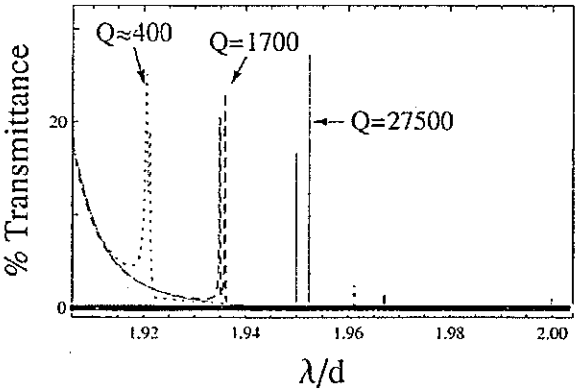

Fig. 9. (Color online) Transmittance and Q factors for a linear waveguide for *TM* incidence with $k_x d/\pi=1$ and $k_y=0$ fixed. The defect size is $r_w=0$ (red/dotted), i.e., cylinder completely removed, $r_w=0.5r$ (blue/dashed), $r_w=0.8r$ (green/thin), and $r_w=r$, i.e., no defect (black/thick). The resonances shift to longer wavelengths as r_w increases.

field and that the woodpile behaves as though it were a uniform medium (details are given in Appendix C).

Initially consider a grating aligned parallel to the x axis. For normal incidence $\mathrm{M}^{EH}=\mathrm{M}^{HE}=0$, consequently the electric and magnetic problems decouple. Further, when $\lambda \gg D$ only the specular order $s=(0,0)$ is required so

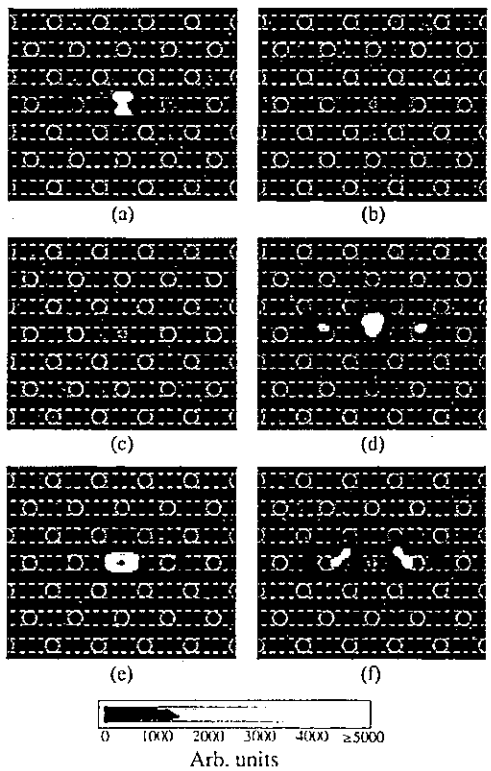

Fig. 10. (Color online) Field intensity in the vicinity of the linear waveguide: (a) $|E_x|^2$ (Media 1), (c) $|E_y|^2$, (e) $|E_z|^2$, (b) $|H_x|^2$, (d) $|H_y|^2$, and (f) $|H_z|^2$. The radius of the defect rod (dashed circle) is $r_w=0.5r$, and the parameters of the incident field are $k_x\pi/d=1$, $k_y=0$, and $\lambda/d=1.936$, i.e., for the resonance indicated in Fig. 9. An animation showing $|E_x|^2$ for the entire unit cell is available online.

that $\mathcal{R}=\mathrm{diag}[R^{EE}R^{HH}]$ for scalars R^{EE} and R^{HH}, and similarly $\mathcal{T}=\mathrm{diag}[T^{EE}T^{HH}]$. For R^{EE} it suffices to use the monopole approximation in Eq. (19), i.e., using only the $m=0$ multipole order, while for R^{HH} the dipole approximation (using the $m=-1,0,1$ multipoles) is needed. For each cylinder l we specify a permittivity ε_l relative to the background, with permeability μ_l taken to be 1, and define the filling fraction $f_l=\pi r_l^2/(dh)$, where r_l is the radius and h is the thickness of the unit cell [see Fig. 3(b)]. One finds

$$R^{EE}\approx\frac{ikh}{2}\frac{1}{N_c}\sum_{l=1}^{N_c}f_l(\varepsilon_l-1), \tag{37}$$

$$R^{HH}\approx-\frac{ikh}{2}\frac{1}{N_c}\sum_{l=1}^{N_c}\frac{2f_l}{\dfrac{\varepsilon_l+1}{\varepsilon_l-1}-\dfrac{\pi h}{3d}f_l}, \tag{38}$$

$$T^{EE}\approx 1+R^{EE}, \tag{39}$$

and

$$T^{HH}\approx 1+R^{HH}. \tag{40}$$

For a grating aligned along the y axis, the expressions for R^{EE} and R^{HH} are simply interchanged. For a pair of non-interpenetrating orthogonal gratings, the stacking recurrences [Eqs. (24)] then give

$$R^{EE}_{\mathrm{pair}}=R^{HH}+T^{EE}T^{HH}R^{EE}/(1-R^{EE}R^{HH}), \tag{41}$$

$$=R^{HH}+R^{EE}+O(k^2), \tag{42}$$

$$\approx R^{HH}_{\mathrm{pair}}, \tag{43}$$

and similarly $T^{EE}_{\mathrm{pair}}\approx T^{HH}_{\mathrm{pair}}$. Consequently, the scattering matrices for a stack of such pairs approach a scalar multiple of the identity matrix, irrespective of whether successive pairs are interleaved. Thus at long wavelengths, in view of Eqs. (33), (34), and (36), the transmittance and reflectance of a woodpile do not depend appreciably on the polarization of the incident field.

For sufficiently large λ, the Fabry–Pérot reflection coefficient for a slab of thickness h and permittivity ε may be approximated using $R\approx(ikh/2)(\varepsilon-1)$. Comparing this with the asymptotic expressions of Eqs. (37) and (38), we conclude that each layer becomes indistinguishable from a rectangular slab having a permittivity of

$$\varepsilon_{TE}-1=\frac{1}{N_c}\sum_{l=1}^{N_c}f_l(\varepsilon_l-1) \tag{44}$$

for TE incidence and

$$\varepsilon_{TM}-1=\frac{1}{N_c}\sum_{l=1}^{N_c}\frac{2f_l}{\dfrac{\varepsilon_l+1}{\varepsilon_l-1}-\dfrac{\pi h}{3d}f_l} \tag{45}$$

for TM incidence, with the roles of ε_{TE} and ε_{TM} interchanged if the cylinders are instead aligned parallel to the y axis.

Similarly, a slab of thickness (h_1+h_2) and permittivity

$$\varepsilon_{\mathrm{pair}}-1=[h_1(\varepsilon_{TE}-1)+h_2(\varepsilon_{TM}-1)]/(h_1+h_2) \tag{46}$$

can be substituted for an orthogonal pair of gratings. Equation (46) is the linear mixing formula and depends neither on the polarization of the incident field nor on the order in which the two gratings are stacked.

When $d=h$ and $N_c=1$, one expects Eq. (45) to reduce to the Maxwell–Garnett formula [30]:

$$\varepsilon_{\mathrm{eff}}=1+\frac{2f_1}{\dfrac{\varepsilon_1+1}{\varepsilon_1-1}-f_1}. \tag{47}$$

The apparent discrepancy of $\pi/3$ arises because the asymptotic form of the grating lattice sum S_2 is given by $S_2\approx 4\pi i/3(kd)^2$, which does not take into account the evanescent coupling that occurs between the layers of the woodpile. This can be rectified for 2D infinite stacks by instead using the array sum [31] $\tilde{S}_2=3S_2/\pi$.

Figure 11 compares the transmittance of a 16-layer woodpile (normal incidence, $N_c=1$, $h=d$, $n_l=3$) calculated using Eqs. (21) and (22), which we take to be exact, with that of a 16-layer stack of uniform slabs where the thick-

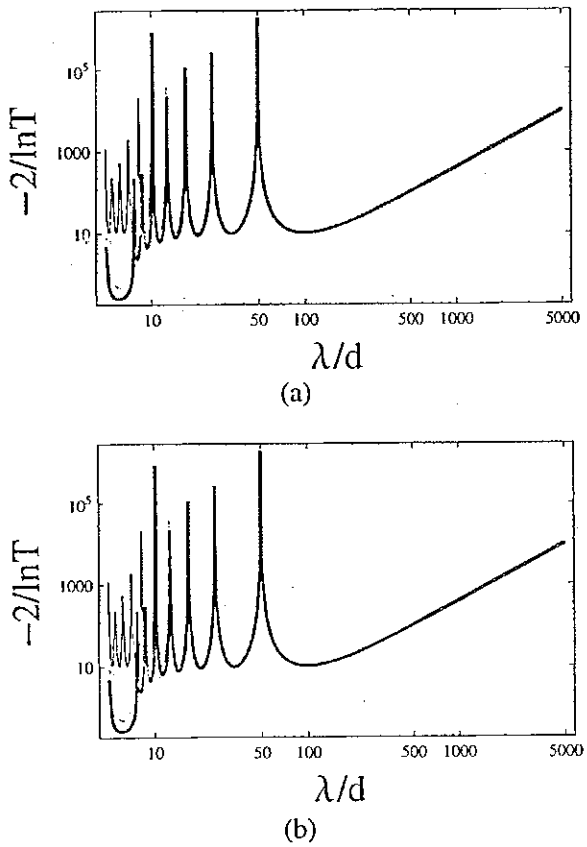

Fig. 11. (Color online) Transmittance of a 16-layer woodpile for (a) TE and (b) TM incidence. The incident field is perpendicular to the grating plane. The exact values are shown in red/thick, while the blue/thin curve corresponds to a 16-layer stack of alternating homogeneous slabs, each with thickness $h=d$ and permittivity given either by Eq. (44) or Eq. (45). The green/dashed curve corresponds to a single slab of thickness $8d$ with permittivity given by Eq. (46).

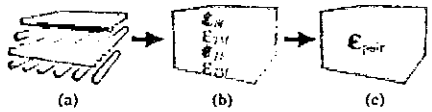

Fig. 12. (Color online) (a) Four-layer photonic woodpile and successive approximations using (b) alternating slabs and (c) a single block of dielectric. For the woodpile parameters given in Section 3.C, the approximations above can be used in place of a woodpile when $\lambda/d>10$.

ness of each slab is h and the permittivity is taken to be the effective permittivity of the corresponding layer of the woodpile, i.e., using Eq. (44) or Eq. (45) as depicted in Fig. 12(b). There is excellent agreement for $\lambda/d>10$; evidently the cylinders are too fine to be resolved so that each layer homogenizes to a slab of uniform dielectric having the same thickness as the layer. In addition, Fig. 11 also includes the transmittance of a single dielectric slab of thickness $h=16d$ and permittivity given by Eq. (46), as depicted in Fig. 12(c). Again, good agreement with the exact values is seen, which suggests that the stripe pattern created by the layers also becomes indistinct.

4. CONCLUSION

It is expected that scattering losses due to extrinsic factors such as surface roughness will be less deleterious for woodpiles than for 2D PCs, owing to the omnidirectional bandgap of the woodpile, particularly in the 'slow-light' regime where the amount of parasitic scattering increases sharply. We have presented extensions to the multipole method that are needed in order to model rod-type defects in woodpiles. This entails generalizing the grating super cell to allow for more than one cylinder. To demonstrate our implementation, a brief characterization of both a CROW and a linear waveguide has been performed, where each defect layer was surrounded by a woodpile cladding. For both types of waveguides, the transmission spectra over the bandgap frequencies of the host woodpile revealed the existence of '*TM*-like' waveguiding modes that could be excited by a *TM* polarized incoming field. Changing the size of the defect rod proved to be an effective way of controlling the Q factors. In particular, the linear waveguide modeled here supports waveguide modes that may have sufficiently small volumes to enable low-loss waveguiding over useful distances. It was observed that 28 layers were needed for the chalgogenide woodpile ($n=2.64$) to behave like a bandgap material. This is reminiscent of the work of [10], where it was determined that for a GaAs woodpile ($n\approx3.38$) about 25 layers are needed to achieve lossless waveguiding over a length of 500 μm.

The high Q factors make it challenging to locate transmission resonances, particularly for the linear waveguide as it requires a large unit cell for the defect layer. Nonetheless, there are a number of complementary approaches, such as that outlined in Section 3.B, that may be better suited to types of waveguides considered in this paper. In particular, the method of fictitious source superposition [23,24] may be a more expedient approach to modeling a linear waveguide as it obviates the need for a large unit cell.

The multipole method not only reduces the computational burden of modeling these types of structures but also permits asymptotic analyses. Effective electric permittivities that are applicable for sufficiently long wavelengths when the incident field is normal to the grating plane were derived for the woodpile and for the individual layers. In the future, we will investigate the long wavelength behavior of the woodpile for conical incidence.

APPENDIX A: ELABORATION OF THE RAYLEIGH IDENTITY AND SCATTERING MATRIX EXPRESSIONS

For a source point $\mathbf{r}'$ on the boundary C_j [see Fig. 2(a)], the value of the Green's function G [defined implicitly by Eq. (9)] at a point $\mathbf{r}$ in the vicinity of cylinder l relative to the center $\mathbf{c}_l$, is given by

$$G(\mathbf{r}-\mathbf{r}')=-\frac{i}{4}\sum_{m=-\infty}^{\infty}H_m(k_\perp r)J_m(k_\perp r')\exp(im\theta_{\mathbf{r}})\times\exp(-im\theta_{\mathbf{r}'})+\sum_{n=-\infty}^{\infty}J_n(k_\perp r)\exp(in\theta_{\mathbf{r}})\times\sum_{s=-\infty}^{\infty}S_{n-s}J_s(kr')\exp(-is\theta_{\mathbf{r}'}) \tag{A1}$$

for $j=l$, and by

$$G(\mathbf{r}_l-\mathbf{r}_j'-\mathbf{c}_j+\mathbf{c}_l)=-\frac{i}{4}\sum_{m=-\infty}^{\infty}J_m(k_\perp r_l)\exp(im\theta_{\mathbf{r}_l})\times\sum_{s=-\infty}^{\infty}S_{m-s}^{lj}J_s(kr_j')\exp(-is\theta_{\mathbf{r}_j'}) \tag{A2}$$

for $j\neq l$, where $\theta_{\mathbf{a}}=\arg(\mathbf{a})$. Also,

$$S_m=\sum_{n\neq0}H_m(k_\perp|\mathbf{c}_n|)e^{i\beta_0 nD}\exp[im\theta_{\mathbf{c}_n}], \tag{A3}$$

and

$$S_m^{lj}=\sum_{n=-\infty}^{\infty}H_m(k_\perp|\mathbf{c}_n^{lj}|)e^{i\beta_0 nD}\exp[im\theta_{\mathbf{c}_n^{lj}}], \tag{A4}$$

where $\mathbf{c}_n=nD\hat{\mathbf{x}}$ and $\mathbf{c}_n^{lj}=\mathbf{c}_j-\mathbf{c}_l+\mathbf{c}_n$. The multipole scattering matrix appearing in the Rayleigh identity [Eq. (12)] is then given by $\mathcal{S}=\mathrm{diag}[\mathsf{S},\mathsf{S}]$, $\mathsf{S}=[\mathsf{S}^{lj}]$, $\mathsf{S}^{lj}=[S_{n-m}^{lj}]$. In addition, the multipole change of basis matrices [see Eq. (12) and Eq. (17)] are defined as $\mathcal{J}^{\pm}=\mathrm{diag}[[\mathsf{J}^{l,\pm}][\mathsf{J}^{l,\pm}]]$, $\mathsf{J}^{l,\pm}=[J_{nq}^{l,\pm}]$,

$$\mathcal{K}=[(\mathcal{K}^-)^T(\mathcal{K}^+)^T]^T,\qquad \mathcal{K}^{\pm}=\begin{bmatrix}\mathsf{K}^{1,\pm}&\cdots&\mathsf{K}^{N_c,\pm}&0&\cdots&0\\0&\cdots&0&\mathsf{K}^{1,\pm}&\cdots&\mathsf{K}^{N_c,\pm}\end{bmatrix}, \tag{A5}$$

$\mathsf{K}^{l,\pm}=[K_{qn}^{l,\pm}]$, and $K_{qn}^{l,\pm}=(\pm1)^n\exp[\mp in\arg(\gamma_s+i\beta_q)]\times\exp(-i\beta_q c_l)$. Accordingly, the symmetrized versions of the multipole transformation matrices [see Eq. (19)] are $\mathcal{J}^{s/a}=\mathrm{diag}[\mathcal{J}^-\pm\mathcal{J}^+\ \mathcal{J}^-\mp\mathcal{J}^+]$ and $\mathcal{K}^{s/a}=\mathrm{diag}[\mathcal{K}^-\pm\mathcal{K}^+\ \mathcal{K}^-\mp\mathcal{K}^+]$.

As was discussed in Section 2.B, the above matrices appear as folded quantities in the final expressions for the scattering matrices [i.e. Eqs. (21) and (22)]. Specifically,

$$\tilde{\mathcal{L}}^{s/a}=\begin{bmatrix}\tilde{\mathsf{M}}^{EE}+\tilde{\mathsf{S}}^{s/a}\varepsilon^{s/a} & \tilde{\mathsf{M}}^{EH}\\ \tilde{\mathsf{M}}^{HE} & \tilde{\mathsf{M}}^{HH}+\tilde{\mathsf{S}}^{a/s}\varepsilon^{a/s}\end{bmatrix}^{-1}, \tag{A6}$$

$\tilde{\mathsf{S}}^{s/a}=[\tilde{S}^{lj,s/a}]$, $\tilde{S}^{lj,s/a}=[S^{lj}_{n-m}\pm(-1)^m S^{lj}_{n+m}]$, $\varepsilon^s=\mathrm{diag}[\mathrm{diag}[\varepsilon,\mathrm{I}]]$, $\varepsilon^a=\mathrm{diag}[\mathrm{diag}[\mathrm{I},\varepsilon]]$, $\varepsilon=\mathrm{diag}[\varepsilon_m]$,

$$\varepsilon_m=\begin{cases}1/2, & \text{for } m=0,\\ 1, & \text{for } m>0\end{cases}$$

and $\mathsf{M}^{EE/HH}$ are the blocks of $\mathcal{M}$ (see Appendix B).

In deriving the Rayleigh identity, the longitudinal (i.e., x) components $\delta_q^{\pm,V}$ of the incoming fields were required [see Eq. (11)]. These are obtained using $\mathcal{D}^-=\mathsf{Z}\mathsf{X}^-\mathcal{F}_I^-$ and $\mathcal{D}^+=\mathsf{Z}\mathsf{X}^+\mathcal{F}_I^+$, where $\mathcal{D}^\pm=[(\mathsf{D}^{\pm,E})^T\,(\mathsf{D}^{\pm,H})^T]^T$, $\mathsf{D}^{\pm,E/H}=[\delta_q^{\pm,E/H}]$, and where $\mathsf{Z}_{11}=\mathsf{Z}_{22}^{-1}=\mathrm{diag}[(\mu_b/\varepsilon_b)^{1/4}]$, $\mathsf{Z}_{12}=\mathsf{Z}_{21}=0$, $\mathsf{X}^-_{11}=-\mathsf{X}^-_{22}=-\mathrm{diag}[\xi_s^{-1/2}\beta_q(\alpha_p^2+\beta_q^2)^{-1/2}]$, and $\mathsf{X}^-_{12}=\mathsf{X}^-_{21}=\mathrm{diag}[\xi_s^{1/2}\alpha_p(\alpha_p^2+\beta_q^2)^{-1/2}]$. Similar expressions exist for the blocks of X^+; however, they are not needed here (consult [25]). It follows that the change of coordinates matrices in Eq. (18) are $\mathcal{Z}=\mathrm{diag}[\mathsf{Z},\mathsf{Z}]$ and $\hat{\mathcal{X}}=\mathrm{diag}[\mathsf{X}^-,\mathsf{X}^+]$, which, after the symmetry folding procedure [see Eqs. (19), (21), and (22)] simplifies to $\mathcal{X}=\mathrm{diag}[\mathsf{X},\mathsf{X}]$, with $\mathsf{X}=\mathsf{X}^-$.

APPENDIX B: EXPRESSIONS FOR THE BOUNDARY CONDITIONS

The matrix $\mathcal{M}$ encapsulating the boundary conditions [see Eq. (15)] is a 2 by 2 block matrix, and we use superscripts E and H to label the blocks so that

$$\mathcal{M}=\begin{bmatrix}\mathsf{M}^{EE} & \mathsf{M}^{EH}\\ \mathsf{M}^{HE} & \mathsf{M}^{HH}\end{bmatrix}. \tag{B1}$$

Each block is diagonal with N_c partitions, where N_c is the number of cylinders in the grating unit cell. We use l to index the cylinders and n to index the elements of the partition. In addition, the label 'II' denotes quantities that depend on the material properties of cylinder l, while 'I' denotes quantities that depend on the properties of the background region. If the radius of cylinder l is a_l, then the entries on the diagonal of each block are

$$\mathsf{M}^{EE}_{l,n}=\frac{\eta_2(\mathrm{I})\eta_3(\mathrm{I})H_n(k_{\perp\mathrm{I}}r_l)J_n(k_{\perp\mathrm{I}}r_l)}{\Delta}\times\left\{\frac{[\eta_1(\mathrm{I})-\eta_1(\mathrm{II})]^2}{\eta_2(\mathrm{I})\eta_3(\mathrm{I})}-J_2H_3\right\}, \tag{B2}$$

$$\mathsf{M}^{HH}_{l,n}=\frac{\eta_2(\mathrm{I})\eta_3(\mathrm{I})H_n(k_{\perp\mathrm{I}}r_l)J_n(k_{\perp\mathrm{I}}r_l)}{\Delta}\times\left\{\frac{[\eta_1(\mathrm{I})-\eta_1(\mathrm{II})]^2}{\eta_2(\mathrm{I})\eta_3(\mathrm{I})}-J_3H_2\right\}, \tag{B3}$$

$$\mathsf{M}^{EH}_{l,n}=\frac{[\eta_1(\mathrm{I})-\eta_1(\mathrm{II})]\eta_2(\mathrm{I})\eta_3(\mathrm{I})}{\Delta}\times\frac{2k\mu_1}{\pi k_{\perp\mathrm{I}}^2 r_l}, \tag{B4}$$

$$\mathsf{M}^{HE}_{l,n}=-(\varepsilon_1/\mu_1)\mathsf{M}^{EH}_{l,n}, \tag{B5}$$

with $k_{\perp i}^2=k^2\varepsilon_i\mu_i-\alpha_p^2$, $\eta_1(j)=-\alpha_p n/[(k_{\perp j})^2 r_l]$, $\eta_2(j)=-ik\mu_j/k_{\perp j}$, $\eta_3(j)=ik\varepsilon_j/k_{\perp j}$,

$$\Delta=J_n(k_{\perp\mathrm{I}}r_l)^2\eta_2(\mathrm{I})\eta_3(\mathrm{I})\times\left\{\frac{[\eta_1(\mathrm{I})-\eta_1(\mathrm{II})]^2}{\eta_2(\mathrm{I})\eta_3(\mathrm{I})}-J_2J_3\right\},$$

$$J_j=\frac{J_n'(k_{\perp\mathrm{I}}r_l)}{J_n(k_{\perp\mathrm{I}}r_l)}-\frac{\eta_j(\mathrm{II})J_n'(k_{\perp\mathrm{II}}r_l)}{\eta_j(\mathrm{I})J_n(k_{\perp\mathrm{II}}r_l)}, \tag{B6}$$

and

$$H_j=\frac{H_n'(k_{\perp\mathrm{I}}r_l)}{H_n(k_{\perp\mathrm{I}}r_l)}-\frac{\eta_j(\mathrm{II})J_n'(k_{\perp\mathrm{II}}r_l)}{\eta_j(\mathrm{II})J_n(k_{\perp\mathrm{II}}r_l)}.$$

APPENDIX C: DERIVATION OF THE ASYMPTOTIC EXPRESSIONS OF SECTION 3.C

If $\mathcal{R}'=\mathrm{diag}[R'^{EE}R'^{HH}]$ and $\mathcal{T}'=\mathrm{diag}[T'^{EE}T'^{HH}]$ are the scattering matrices for a y aligned grating, it follows readily from Eq. (19) that for normal incidence and $\lambda/d\gg D$,

$$R^{EE}\approx R'^{HH}\approx-\frac{1}{2kD}\times[\mathcal{K}^{\ominus}(\mathsf{M}^{EE}+\mathsf{S})^{-1}\mathcal{J}^{\oplus}-\mathcal{K}^{\ominus}(\mathsf{M}^{EE}+\mathsf{S})^{-1}\mathcal{J}^{\oplus}], \tag{C1}$$

$$R^{HH}\approx R'^{EE}\approx-\frac{1}{2kD}\times[\mathcal{K}^{\ominus}(\mathsf{M}^{HH}+\mathsf{S})^{-1}\mathcal{J}^{\oplus}-\mathcal{K}^{\ominus}(\mathsf{M}^{HH}+\mathsf{S})^{-1}\mathcal{J}^{\oplus}], \tag{C2}$$

$$T^{EE}\approx T'^{HH}\approx1-\frac{1}{2kD}\times[\mathcal{K}^{\oplus}(\mathsf{M}^{EE}+\mathsf{S})^{-1}\mathcal{J}^{\oplus}+\mathcal{K}^{\ominus}(\mathsf{M}^{EE}+\mathsf{S})^{-1}\mathcal{J}^{\ominus}], \tag{C3}$$

and

$$T^{HH}\approx T'^{EE}\approx1-\frac{1}{2kD}\times[\mathcal{K}^{\oplus}(\mathsf{M}^{HH}+\mathsf{S})^{-1}\mathcal{J}^{\oplus}+\mathcal{K}^{\ominus}(\mathsf{M}^{HH}+\mathsf{S})^{-1}\mathcal{J}^{\ominus}], \tag{C4}$$

where $\mathcal{K}^{\oplus/\ominus}=\mathcal{K}^-\pm\mathcal{K}^+$ and $\mathcal{J}^{\oplus/\ominus}=\mathcal{J}^-\pm\mathcal{J}^+$. In the above we have used the fact that $\mathcal{K}^s\mathcal{L}\mathcal{J}^a=\mathcal{K}^a\mathcal{L}\mathcal{J}^s=0$ for up–down symmetric gratings. Evaluation of the matrix inversions requires the long wavelength approximations for Eqs. (B2) and (B3), and these in turn are deduced from the Taylor series expansions, which result in

$$\mathsf{M}^{EE}_{l,0}\approx\frac{4i}{f_l\alpha^2(\varepsilon_l-1)}, \tag{C5}$$

$$\mathsf{M}_{l,1}^{EE} \approx \mathsf{M}_{l,0}^{HH} = \frac{32\pi i}{f_l^2 \alpha^4 (\varepsilon_l - 1)}, \tag{C6}$$

and

$$\mathsf{M}_{l,1}^{HH} \approx \mathsf{M}_{l,0}^{EE}(\varepsilon_l + 1), \tag{C7}$$

where $\alpha = k\sqrt{dh}$. Along with the assumption that there is only weak disorder in the values of ε_l (hence $M_{l,n}^{EE/HH} \approx M_{j,n}^{EE/HH}$ for any two cylinders l and j) and in the cylinder offsets $\mathbf{c}_l$, Eqs. (C5)–(C7) enable each matrix inversion to be carried out analytically. Using the approximations for the lattice sums given in [16], one finds after simplification

$$\mathcal{K}^{\ominus}(\mathsf{M}^{EE/HH} + \mathsf{S})^{-1}\mathcal{J}^{\ominus} \approx 4\sum_{l=1}^{N_c} \frac{1}{M_{l,0}^{EE/HH}} \tag{C8}$$

for both the monopole and dipole approximations. Also, for the monopole case

$$\mathcal{K}^{\ominus}(\mathsf{M}^{EE/HH} + \mathsf{S})^{-1}\mathcal{J}^{\ominus} = 0, \tag{C9}$$

while for the dipole case

$$\mathcal{K}^{\ominus}(\mathsf{M}^{EE/HH} + \mathsf{S})^{-1}\mathcal{J}^{\ominus} \approx 8\sum_{l=1}^{N_c} \frac{1}{M_{l,1}^{EE/HH} - \dfrac{4\pi i}{3\alpha^2}}. \tag{C10}$$

For the monopole approximations we then have

$$R^{EE} \approx \frac{ikh}{2}\frac{1}{N_c}\sum_{l=1}^{N_c} f_l(\varepsilon_l - 1) = O(\alpha), \tag{C11}$$

$$T^{EE} \approx 1 + R_0^{EE}, \tag{C12}$$

$$R^{HH} \approx \frac{ikh}{2}\left(\frac{-\alpha^2}{8\pi N_c}\right)\sum_{l=1}^{N_c} f_l^2(\varepsilon_l - 1) = O(\alpha^3), \tag{C13}$$

and

$$T^{HH} \approx 1 - R_0^{HH}. \tag{C14}$$

Note that Eq. (C8) contains only monopole terms, i.e., $M_{l,0}^{EE/HH}$, while Eq. (C10) contains only dipole terms. Thus the terms in Eqs. (C1)–(C4) involving $\mathcal{K}^{\ominus}$ and $\mathcal{J}^{\ominus}$ may be viewed as the monopole approximations, while those involving $\mathcal{K}^{\ominus}$ and $\mathcal{J}^{\ominus}$ are dipole corrections, so that we may write for the dipole approximation of R^{EE}

$$R^{EE} \approx R_0^{EE} + \Delta^{EE} \approx R_0^{EE}, \tag{C15}$$

where R_0^{EE} is the monopole approximation given by Eq. (C11) and

$$\Delta^{EE} \approx \frac{ikh}{2}\left(\frac{-2\alpha^2}{N_c}\right)\sum_{l=1}^{N_c} \frac{f_l^2}{\dfrac{8\pi}{\varepsilon_l - 1} - \dfrac{\pi}{3}(khf_l)^2} = O(\alpha^3) \tag{C16}$$

is the dipole correction. Similarly,

$$R^{HH} \approx R_0^{HH} + \Delta^{HH}, \tag{C17}$$

with

$$\Delta^{HH} \approx \frac{ikh}{2}\left(\frac{2}{N_c}\right)\sum_{l=1}^{N_c} \frac{f_l}{\dfrac{\varepsilon_l + 1}{\varepsilon_l - 1} - \dfrac{\pi h}{3d}f_l} = O(\alpha). \tag{C18}$$

Analogous relationships also hold for T_{EE} and T_{HH}. Equations (C15) and (C17) justify our claim that only the monopole approximations are needed to compute R^{EE} and T^{EE}, while for R^{HH} and T^{HH} the dipole approximations must be used instead.

ACKNOWLEDGMENTS

This work was produced with the assistance of the Australian Research Council under its Centres of Excellence Program. Many of the results in this paper were obtained using the high-performance computing facilities provided by *ac3*. Dr. C. G. Poulton acknowledges the support of a start-up grant awarded by the University of Technology, Sydney.

REFERENCES

1. E. Yablonovitch, "Inhibited spontaneous emission in solid-state physics and electronics," Phys. Rev. Lett. 58, 2059–2062 (1987).
2. J. D. Joannopoulos, S. G. Johnson, J. N. Winn, and R. D. Meade, *Photonic Crystals: Molding the Flow of Light* (Princeton Univ. Press, 2008).
3. H. S. Sözüer and J. P. Dowling, "Photonic band calculations for woodpile structures," J. Mod. Opt. 41, 231–239 (1994).
4. G. A. Ozin, "The photonic opal: the jewel in the crown of optical information processing," Chem. Commun. (Cambridge) 21, 2639–2643 (2003).
5. K. Busch and S. John, "Photonic bandgap formation in certain self-organizing systems," Phys. Rev. E 58, 3896–3908 (1998).
6. A. Taflove and S. C. Hagness, *Computational Electrodynamics: The Finite-Difference Time-Domain Method* (Artech House, 2005).
7. S. G. Johnson and J. D. Joannopoulos, "Block-iterative frequency-domain methods for Maxwell's equations in a plane-wave basis," Opt. Express 8, 173–190 (2001).
8. A. Feigel, M. Veinger, B. Sfez, A. Arsh, M. Klebanov, and V. Lyubin, "Three-dimensional simple cubic woodpile photonic crystals made from chalcogenide glasses," Appl. Phys. Lett. 83, 4480–4482 (2003).
9. A. Feigel, Z. Kotler, B. Sfez, A. Arsh, M. Klebanov, and V. Lyubin, "Interference lithography for 3D photonic band gap crystal layer by layer fabrication," in *Materials Research Society Symposium Proceedings*, 2001, E. D. Jones, O. Manasreh, K. D. Choquette, D. J. Friedman, and D. K. Johnstone, eds.,Vol. 692, K2.9.1.
10. M. Imada, L. H. Lee, M. Okano, S. Kawashima, and S. Noda, "Development of three-dimensional photonic-crystal waveguides at optical-communication wavelengths," Appl. Phys. Lett. 88, 171107 (2006).
11. J. G. Fleming, S. Y. Lin, I. El-Kady, R. Biswas, and K. M. Ho, "All-metallic three-dimensional photonic crystals with a large infrared bandgap," Nature 417, 52–55 (2002).
12. S. Wu, J. Serbin, and M. Gu, "Two-photon polymerization for three-dimensional microfabrication," J. Photochem. Photobiol., A 181, 1–11 (2006).
13. E. Nicoletti, G. Zhou, B. Jia, M. J. Ventura, D. Bulla, B. Luther-Davies, and M. Gu, "Observation of multiple higher-order stopgaps from three-dimensional chalcogenide glass photonic crystals," Opt. Lett. 33, 2311–2313 (2008).

14. G. H. Smith, L. C. Botten, R. C. McPhedran, and N. A. Nicorovici, "Cylinder gratings in conical incidence with applications to woodpile structures," Phys. Rev. E **67**, 056620 (2003).
15. B. Gralak, M. de Dood, G. Tayeb, S. Enoch, and D. Maystre, "Theoretical study of photonic bandgaps in woodpile crystals," Phys. Rev. E **67**, 066601 (2003).
16. A. A. Asatryan, P. A. Robinson, L. C. Botten, R. C. McPhedran, N. A. Nicorovici, and C. M. de Sterke, "Effects of disorder on wave propagation in two-dimensional photonic crystals," Phys. Rev. E **60**, 6118–6127 (1999).
17. R. C. McPhedran, C. G. Poulton, N. A. Nicorovici, and A. B. Movchan, "Low frequency corrections to the static effective dielectric constant of a two-dimensional composite material," Proc. R. Soc. London, Ser. A **452**, 2231–2245 (1996).
18. J. Cheng, R. Hong, and J. Yang, "Analysis of planar defect structures in three-dimensional layer-by-layer photonic crystals," J. Appl. Phys. **104**, 063111 (2008).
19. M. Okano, S. Kako, and S. Noda, "Coupling between a point-defect cavity and a line-defect waveguide in three-dimensional photonic crystal," Phys. Rev. B **68**, 235110 (2003).
20. G. von Freymann, S. Wong, G. A. Ozin, S. John, F. Pérez-Willard, M. Deubel, and M. Wegener, in *Conference on Lasers and Electro-Optics, 2005*, CTuU5, pp. 1002–1004.
21. F. García-Santamaría, M. Xu, V. Lousse, S. Fan, P. V. Braun, and J. A. Lewis, "A germanium inverse woodpile structure with a large photonic bandgap," Adv. Mater. **19**, 1567–1570 (2007).
22. E. Centeno and D. Felbacq, "Rigorous vector diffraction of electromagnetic waves by bidimensional photonic crystals," J. Opt. Soc. Am. A **17**, 320–327 (2000).
23. S. Wilcox, L. C. Botten, R. C. McPhedran, C. G. Poulton, and C. M. de Sterke, "Modeling of defect modes in photonic crystals using the fictitious source superposition method," Phys. Rev. E **71**, 056606 (2005).
24. L. C. Botten, K. B. Dossou, S. Wilcox, R. C. McPhedran, C. M. de Sterke, N. A. Nicorovici, and A. A. Asatryan, "Highly accurate modelling of generalized defect modes in photonic crystals using the fictitious source superposition method," Microwave Opt. Technol. Lett. **1**, 133–145 (2006).
25. G. H. Smith, L. C. Botten, R. C. McPhedran, and N. A. Nicorovici, "Cylinder gratings in conical incidence with applications to modes of air-cored photonic crystal fibers," Phys. Rev. E **66**, 056604 (2002).
26. L. C. Botten, N. A. Nicorovici, A. A. Asatryan, R. C. McPhedran, C. M. de Sterke, and P. A. Robinson, "Formulation for electromagnetic scattering and propagation through grating stacks of metallic and dielectric cylinders for photonic crystal calculations. Part I. Method," J. Opt. Soc. Am. A **17**, 2165–2177 (2000).
27. A. Moroz, "Exponentially convergent lattice sums," Opt. Lett. **26**, 1119–1121 (2001).
28. B. Gralak, S. Enoch, and G. Tayeb, "From scattering or impedance matrices to Bloch modes of photonic crystals," J. Opt. Soc. Am. A **19**, 1547–1554 (2002).
29. A. Modinos, N. Stefanou, and V. Yannopapas, "Applications of the layer-KRR method to photonic crystals," Opt. Express **8**, 197–202 (2001).
30. J. C. Maxwell Garnett, "Colours in metal glasses and in metallic films," Philos. Trans. R. Soc. London, Ser. A **203**, 385–420 (1904).
31. N. A. Nicorovici, R. C. McPhedran, and L. C. Botten, "Photonic bandgaps for arrays of perfectly conducting cylinders," Phys. Rev. E **52**, 1135–1145 (1995).